Phosphoproteomics of patient-derived xenographs identifies targets and markers associated with sensitivity and resistance to EGFR blockade in colorectal cancer

Title: Phosphoproteomics of PDXs identifies targets and markers associated with sensitivity and resistance to EGFR blockade in colorectal cancer

Authors: *Robin Beekhof[1,2], Andrea Bertotti[3,4], Franziska Böttger[1,2,5], Valentina Vurchio[3,4], Francesca Cottino[3], Eugenia R. Zanella[3], Giorgia Migliardi[3,4], Marco Viviani[3,4], Elena Grassi[3,4], Barbara Lupo[3], Alex A. Henneman[1,2], Jaco C. Knol[1,2], Thang V. Pham[1,2], Richard de Goeij-de Haas[1,2], Sander R. Piersma[1,2], Mariette Labots[1], Henk M.W. Verheul[1,6], Livio Trusolino[3,4], Connie R. Jimenez[1,2]***

Affiliations:

[1]Amsterdam UMC, Vrije Universiteit Amsterdam, Medical Oncology, Cancer Center Amsterdam, De Boelelaan 1117, 1081 HV, Amsterdam, the Netherlands.

[2]Amsterdam UMC, Vrije Universiteit Amsterdam, OncoProteomics Laboratory, Cancer Center Amsterdam, De Boelelaan 1117, 1081 HV, Amsterdam, the Netherlands.

[3]Candiolo Cancer Institute – FPO IRCCS, 10060 Candiolo, Torino, Italy.

[4]Department of Oncology, University of Torino, 10060 Candiolo, Torino, Italy.

[5]Division of Molecular Carcinogenesis, The Netherlands Cancer Institute, Oncode Institute, 1066 CX, Amsterdam, the Netherlands.

[6]Department of Medical Oncology, Erasmus MC Cancer Institute, Erasmus University Medical Center Rotterdam, Dr. Molewaterplein 40, 3015 GD, Rotterdam, The Netherlands

*Corresponding author. Phone: +31 20 444 2340; E-mail: c.jimenez@amsterdamumc.nl

One Sentence Summary: Phosphoproteomics on patient-derived xenografts of metastatic colorectal cancer provided insight on the primary response to EGFR blockade.

Abstract: Epidermal growth factor receptor (EGFR) is a well-exploited therapeutic target in metastatic colorectal cancer (mCRC). Unfortunately, not all patients benefit from current EGFR inhibitors . Mass spectrometry-based proteomics and phosphoproteomics were performed on 30 genomically and pharmacologically characterized mCRC patient-derived xenografts (PDXs) to investigate the molecular basis of response to EGFR blockade and identify alternative drug targets to overcome resistance. Both the tyrosine and global phosphoproteome as well as the proteome harbored distinctive response signatures. We found increased pathway activity related to MAPK inhibition and abundant tyrosine phosphorylation of cell junction proteins, such as CXADR and CLDN1/3, in sensitive tumors, whereas epithelial-mesenchymal transition and increased MAPK and AKT signaling were more prevalent in resistant tumors. Furthermore, the ranking of kinase activities in single samples confirmed driver activity of ERBB2, EGFR, and MET in cetuximab-resistant tumors. This analysis also revealed high kinase activity of several members of the SRC and Ephrin kinase family in 2 CRC PDX models with genomically unexplained resistance. Inhibition of these hyperactive kinases, alone or in combination with cetuximab, resulted in growth inhibition of ex vivo PDX-derived organoids and in vivo PDXs. Together, these findings highlight the potential value of phosphoproteomics to improve our understanding of anti-EGFR treatment and response prediction in mCRC and bring to the forefront alternative drug targets in cetuximab-resistant tumors.

Main Text:

INTRODUCTION

Epidermal Growth Factor Receptor (EGFR) blocking monoclonal antibodies (mAb) cetuximab and panitumumab belong to the standard therapeutic arsenal for patients with metastatic colorectal cancer (mCRC). Administration of these drugs, regardless of treatment line or chemotherapeutic backbone, has improved response rates and overall survival in this patient population *(1–4)*. Resistance to cetuximab and panitumumab has been partly attributed to oncogenic mutations downstream of EGFR in KRAS proto-oncogene (*KRAS)* exon 2-4, NRAS proto-oncogene (*NRAS)* exon 2-4, or B-Raf proto-oncogene (*BRAF)* V600E. According to the European Society for Medical Oncology (ESMO) and the National Comprehensive Cancer Network (NCCN) guidelines *(5, 6)* patients with these mutations are excluded for treatment with cetuximab or panitumumab. Despite overall treatment benefit in patients without oncogenic mutations in KRAS, NRAS or BRAF (RAS/RAF wild-type), 30% of patients do not receive clinical benefit from anti-EGFR mAb treatment *(7)* due to the high molecular complexity and heterogeneity of these tumors. In addition, patients with RAS/RAF wild-type (WT) tumors located in the right side of the colon respond less to anti-EGFR antibodies compared with patients suffering from left-sided CRC tumors, which are usually more dependent on EGFR signaling due to the different embryological origin of the hindgut *(8)*.

In recent years, genomics has identified several resistance mechanisms and predictive biomarkers in RAS/RAF WT patient-derived xenograft (PDX) models, including MET proto-oncogene (*MET)* and erb-b2 receptor tyrosine kinase 2 (*ERBB2)* amplification and mutations in *ERBB2*, *EGFR*, fibroblast growth factor receptor 1 (*FGFR1)*, platelet derived growth factor receptor alpha (*PDGFRA)*, and mitogen-activated protein kinase kinase 1 (MAP2K1) *(9–11)*. This study extends these findings, using proteomics and phospho-proteomics as a complementary approach to capturing protein expression and activation states globally. Kinases control protein activity and signaling through phosphorylation *(12)*. Thus, unbiased profiling of protein phosphorylation by mass spectrometry (phosphoproteomics) may uncover predictive markers and drug targets *(13–15)*. Specifically, *phosphotyrosine*-based (pTyr) phosphoproteomics provides detailed quantification of tyrosine-phosphorylated proteins that are crucial for cancer proliferation signaling and thereby may be advantageous to understand tyrosine kinase inhibitor responses. Underscoring feasibility of such an approach in the clinical setting, we have previously shown that down-scaling of the pTyr enrichment protocol is accomplishable and can be successfully deployed to uncover patient-specific and drug-associated profiles in small tumor needle biopsies *(16, 17)*.

Large-scale proteomics and global phosphoproteomics studies applied to CRC in a multi-omics context have contributed to describing the molecular landscape of primary *(18)* and metastatic CRC *(19)* and suggested new therapeutic opportunities for patients with tumors that do not harbor druggable mutations *(19)*. A recent proteomic study in two CRC PDX models that had been rendered resistant to cetuximab by continuous antibody treatment highlighted changes in the abundance of EGFR ligands and enrichment of proliferative kinase signatures as correlates of acquired resistance *(20)*. Whereas these analyses emphasized the importance of kinase-substrate correlation networks for prediction of drug sensitivity in patients with mCRC, they did not address the (phospho)proteomic underpinnings of innate sensitivity and resistance to EGFR inhibition on a systematic basis.

In this study, we combined mass-spectrometry-based proteomics with global (TiO2) and pTyr-based phospho-proteomics, to analyze a unique panel of 30 genomically characterized mCRC-PDX tumors annotated for response to cetuximab as seen in the clinic and confirmed in the mouse setting *(10)*. Our findings improve understanding of the mechanisms dictating sensitivity and resistance to EGFR-blockade in mCRC *(9, 10)* and pinpoint actionable kinase activities in individual tumors that provide new treatment options.

RESULTS

Phosphoproteomics profiling of patient-derived xenografts

To explore biological processes associated with sensitivity and resistance to EGFR blockade and to identify candidate markers and alternative drug targets to overcome resistance, mass spectrometry-based phospho-proteomics was performed on a cohort of 10 cetuximab-sensitive and 20 cetuximab-resistant xenograft tumors, as assessed in a mouse clinical trial that recapitulated the clinical treatment outcomes *(9, 10, 21)* (table S1). Out of twenty resistant tumors, three did not display genetic alterations known to affect responsiveness to EGFR blockade in mCRC (fig. S1A). Mass spectrometry-based proteomics, global phosphoproteomics (TiO2), and pTyr-based phosphoproteomics (fig. S1B) were performed on each tumor tissue sample. Data analysis consisted of comparative group-based analysis of cetuximab-sensitive (CS) versus (vs) cetuximab-resistant (CR) tumors and kinase activity ranking analysis of individual resistant tumors to find potential drug targets (fig. S1C).

Histological assessment of hematoxylin and eosin-stained sections indicated an average percentage of 65% epithelial cancer cells, 15% stroma, and 20% necrosis (fig. S2A). Based on this assessment, three samples (CRC0343, CRC0490, CRC1138_Repl1) showed more than 50% necrosis in the histological assessment. Further proteomic analysis of the samples revealed that two conventional markers for necrosis, namely high mobility group box 1 (HMGB1) and peptidylprolyl isomerase A (PPIA), had only medium-to-low protein expression in the tree samples scored as necrotic. Therefore, no samples were excluded based on histological assessment (fig. S2B).

Seven samples were excluded from TiO2 data. Five samples (CRC0177, CRC0196_Repl1, CRC0254, CRC1138_Repl1, CRC1147_Repl1) were excluded due to technical failure, and two samples (CRC0166_Repl1, CRC0219_Repl1) were excluded due to high variation between replicates and low peptide yield (Suppl. Table. 1, fig. S3). In general, biological replicates of PDX tumors (pTyr, 13 replicates; TiO2, 10 replicates; expression, 12 replicates) clustered together in correlation heatmap (fig. S3).

The mCRC-PDX proteome dataset consisted of 5287 identified proteins and the phosphoproteome dataset consisted of 13.110 class-I phospho-sites (8973 pSer, 1066 pThr, and 3073 pTyr) on 15.095 phospho-peptides from 5207 phosphoproteins (1669 pTyr and 3538 global TiO2 capture) including 255 kinases, of which 53 tyrosine kinases, including EGFR (fig. S4 and Suppl. Tables 2-6). Unsupervised clustering using all (phospho-)proteome data did not show sub-clustering of CS and CR tumors (fig. S5), underscoring the heterogeneity and the minor impact of resistance to cetuximab on the profiles.

Differential (phospho)proteome profiles of cetuximab-sensitive and resistant PDX tumors provide insight into molecular determinants of response to cetuximab

Group-based statistics were performed between CS and CR tumors to find discriminative molecular determinants of response (Fig. 1 A, see Suppl. Table 7 for all comparisons for all data types). These comparative analyses revealed 53 (12 pTyr, 41 TiO2) differentially phosphorylated phospho-sites and 53 proteins with differential abundance in CS tumors versus all resistant tumors (CR-ALL); 75 (8 pTyr, 67 TiO2) differentially phosphorylated phospho-sites and 49 proteins in CS versus CR tumors with oncogenic mutations in KRAS, NRAS or BRAF (CR-MUT); and 17 (4 pTyr, 13 TiO2) differentially phosphorylated phospho-sites and 72 proteins in CS tumors versus resistant RAS/RAF WT tumors (CR-WT) (Fig. 1A).

Comparing significant phospho-sites (p-value <0.01, FC > 1.5) from the tree group comparisons (CS vs. CR-ALL, CS vs. CR-MUT, CS vs. CR-WT) shows an overlap of phospho-sites that either fall into a general response signature (CS1/2/3, CR1/2/3) or a signature for either RAS/RAF mutated (CS4, CR4) or wild-type tumors (CS5, CR5) (Fig. 1A, Suppl. Table 8). (Fig. 1A, Suppl. Table 8). Combining this phospho-site signature for clustering showed clear segregation between cetuximab-sensitive and resistant tumors. Although pTyr, global phosphoproteome, and proteome analyses enabled separation according to drug response, they yielded different layers of information: the pTyr signature predominantly consisted of phospho-sites with increased phosphorylation in sensitive tumors, whereas the global TiO2-based signatures contained almost only phospho-sites that were more phosphorylated in resistant tumors. Moreover, the global TiO2 phosphorylation signatures additionally separated CR-MUT from CR-WT tumors. Finally, the protein expression data were analyzed similarly, and they as well separated sensitive tumors from resistant ones, providing a balanced number of proteins with higher expression in either one of the two response classes (Fig. 1B, fig. S6A-C). Suppl. Table 9 summarizes top discriminative proteins; the top 10 proteins for CS tumors include RAB11 family interacting protein 5 (RAB11FIP5), claudin 3 (CLDN3), solute carrier family 16 member 1 (SLC16A1), claudin 1 (CLDN1), SATB homeobox 2 (SATB2), 4-hydroxyphenylpyruvate dioxygenase like (HPDL), serine incorporator 5 (SERINC5), chromodomain helicase DNA binding protein 7 (CHD7), sorting nexin 33 (SNX33), and CXADR Ig-like cell adhesion molecule (CXADR), whereas the top 10 proteins for CR tumors include absent in melanoma 1 like (AIM1L), asparaginase and isoaspartyl peptidase 1 (ASRGL1), claudin 2 (CLDN2), myelin expression factor 2 (MYEF2), TSC22 domain family member 2 (TSC22D2), torsin family 4 member A (TOR4A), ATP binding cassette subfamily C member 3 (ABCC3), LIM domain and actin binding 1 (LIMA1), neural precursor cell expressed developmentally down-regulated 9 (NEDD9), and tight junction protein 1 (TJP1).

Murine proteins from the host mice in PDX (phospho) samples may influence protein/peptide quantification when doing a human-only database search, especially when tumor cell percentage is not high. The samples from the PDX models described here have a relatively high average of 65% epithelial cell content. Still, to underscore the validity of introducing less complexity in the analysis of the phosphoproteomics PDX results by using a human-only database search, we cross-checked results obtained for the differential phosphosites associated with cetuximab sensitivity and resistance against a database search using the combined human and mouse sequences. Suppl. Table 10 shows that the spectrum identifications based on the combined search resulted in precisely the same underlying set of peptide sequences for each phosphosite. However, the quantification of the phosphosites sites was almost wholly derived from the same precursor signals as in the human-only database search. This additional human-mouse combined database search underscored the validity of the differential phosphosites obtained from analyzing PDX phosphoproteomics data search against the human-only database.

Differential (phospho) proteins of all three comparisons (CS compared to either CR-ALL, CR-MUT, or CR-WT) were combined in a protein-protein interaction network (Fig. 2), showing results from the comparison with the largest fold change in case of overlap between comparisons. mRNA expression of both the complete PDX cohort (157 CS and 246 CR previously described PDX tumors, referred to hereafter as RNA400) *(22)*, and the subset of models used in this study (RNAsub), was used to annotate proteins further (fig. S7). Markov clustering combined with gene ontology analysis revealed eight biologically relevant protein clusters (fig. S8). Clusters associated with cetuximab sensitivity were the **"**cell-cell junction organization**"** cluster, containing the cell-cell adhesion molecules CXADR and claudin 1 and 3, and the **"**ribonucleoprotein complex biogenesis**"** cluster with proteins POU class 2 homeobox associating factor 1 (BOB1), DEAD-box helicase 27 (DDX27), DEAD-box helicase 28 (DDX28), ribosome biogenesis regulator 1 homolog (RRS1), dyskerin pseudouridine synthase 1 (DKC1), RNA terminal phosphate cyclase like 1 (RCL1), nucleophosmin 1 (NPM1), and ribosomal L1 domain containing 1 (RSL1D1). Of note, both RNA400 and RNAsub comparisons showed significant higher expression of CXADR in CS models (p-value <0.05). The clusters **"**enzyme-linked receptor protein signaling**"** and **"**type 1 interferon signaling**"** were more associated with cetuximab resistance. The cluster "enzyme-linked receptor protein signaling" included proteins involved in AKT serine/threonine kinase 1 (AKT1) signaling, where the PI3K-PTEN-AKT signaling axis is known to be involved in resistance to EGFR inhibitors *(23)*. One other cetuximab resistance protein that stands out in Fig. 2 is KIAA1522. Although KIAA1522 is an uncharacterized protein with unknown function, high mRNA expression of KIAA1522 has been linked to non-small cell lung cancer as a marker of poor prognosis *(24)*.

Gene-set enrichment analysis (GSEA) on protein expression and RNAsub data revealed oxidative phosphorylation (OXPHOS) as one of the most enriched processes (adj. *P*-value < 0.05) in CS tumors, along with MYC targets and adipogenesis (Fig. 3, fig. S9). Although the latter two processes were also captured at the RNA level, enrichment of OXPHOS was revealed at the protein level only. In addition, enrichment of these processes was more pronounced (in the case of OXPHOS) or unique (in the case of adipogenesis) in the CR-MUT compared to the CR-WT comparison. CR tumors showed strong enrichment of processes associated with epithelial-mesenchymal transition (EMT) at the RNA and protein levels and interferon response-related biology at the protein level only. (Fig. 3, fig. S9).

Post-translational modification signature enrichment analysis (PTM-SEA) of pTyr data revealed enrichment of the fibroblast growth factor 1 (FGF1) pathway (FDR p-value <0.25) in cetuximab-sensitive tumors. In contrast, resistant tumors showed enrichment (FDR p-value <0.05) of the thymic stromal lymphopoietin pathway (TSLP) and ABL proto-oncogene 1(ABL1) (FDR p-value <0.05). Also, neuroblastoma (FDR p-value <0.25) and anti-CD3 perturbation-related biology (FDR p-value <0.25) were enriched more prominently in CR-MUT tumors (Fig. 4). TiO2 data indicated enrichment of AKT serine/threonine kinase 1 (AKT1) in CR tumors that correlates with the earlier findings in the protein-protein interaction of CS versus CR (Fig. 2). In agreement with expectations, comparative analysis of CS versus CR-MUT showed reduced enrichment for many signaling signatures downstream in the Ras/Raf patway, including mitogen-activated protein kinase 1 (MAPK1) (FDR p-value <0.25), mitogen-activated protein kinase 3 (MAPK3) (FDR p-value <0.25), and MAPK activated protein kinase 2 (MAPKAPK2) (FDR p-value <0.05) in CS samples (Fig. 4). Conversely, CS tumors showed a positive enrichment for phosphosite-driven signatures related to the mitogen-activated protein kinase (MEK)1/2 inhibitor U0126 and the p38 MAPK inhibitor losmapimod (Fig. 4). Additionally, enrichment of the TEK receptor tyrosine

kinase (TIE2) pathway, protein kinase C alpha (PRKCA), and, as in the pTyr signature, anti-CD3 perturbation was related to cetuximab resistance (Fig. 4).

In-depth analysis of resistant tumors reveals hyperactive kinases

To investigate whether hyperactive kinases can act as alternative targets for treatment in cetuximab-resistant tumors, a single sample Integrative inferred Kinase Activity (INKA) analysis was performed on all PDX tumors *(15)* (Suppl. Fig 9 and fig. S11). Figure 6A shows the pTyr kinase activities with an overall 25% higher INKA score comparing CS to CR models, including for CS the kinases; EGFR, EPH receptor B2 (EPHB2), EPH receptor B3 (EPHB3), and fyn related Src family tyrosine kinase (FRK) and in CR tumors; cyclin dependent kinase 5 (CDK5), EPH receptor A3 (EPHA3), insulin like growth factor 1 receptor (IGF1R), spleen associated tyrosine kinase (SYK), mitogen-activated protein kinase 14 (MAPK14), ERBB2, erb-b2 receptor tyrosine kinase 3 (ERBB3), and MET. Comparing the INKA score per kinase across all tumors revealed that some tumors had outlier kinase activity (Fig. 5A, fig. S12). These high INKA scores were found in models that harbored previously identified gene amplifications *(10)* in *EGFR* (CRC0098), *MET* (CRC0196), or *ERBB2* (CRC0080, CRC0176). Further underscoring a critical oncogenic driver function for these kinases is the high (number 1) INKA rank number relative to other identified kinases in the amplified PDX models (Fig. 5B, fig. S11, and fig. S12). Previous work showed that these cetuximab-resistant PDX models with gene amplifications respond to specific inhibition of MET (CRC0196) *(25)* or ERBB2 (CRC0080, CRC0176) *(10, 26)* especially in combination with cetuximab, highlighting their potential as alternative targets for combination treatment (fig. S13). Finally, kinase activity analysis of the TiO2 phosphoproteomics data revealed high activity of AKT1 and MAPK3 in resistant models (fig. S11 and fig. S12). These results are in line with previous work showing that AKT inhibition potentiates the effect of cetuximab treatment *(27)*. Altogether, these results indicate the value of phosphoproteomics coupled with INKA analysis of individual cetuximab-resistant tumors to identify hyper-active kinases as targets for treatment.

Hyper-active kinases highlight potential treatment targets

Previous genomic analysis of PDX models CRC0161, displaying EGFR outlier activity (Fig. 5A) and CRC0166 did not identify oncogenic driver alterations that can explain resistance to cetuximab. Therefore, these two models were investigated in functional experiments with drug selection based on their INKA profile. In both models, INKA analysis pinpointed high activity for EGFR, EPHA2, several other ephrin receptors, as well as SRC family tyrosine kinases (Fig. 6A). EPHA2 has been previously implicated in resistance to EGFR inhibition in gefitinib-resistant HCC827 cells *(28)* and high expression of EPHA2 has been correlated with worse clinical prognosis in patients with mCRC treated with cetuximab *(29, 30)*.

Dasatinib is a potent inhibitor of ephrin family kinases, especially EPHA2, as well as SRC family kinases, and inhibits EGFR when used in the high nanomolar range *(31–33)* (Fig. 6B). Therefore, dasatinib was selected to test the potential of these kinases as alternative treatment targets. Viability upon treatment was tested in organoid cultures derived from PDX-model CRC0161, which showed INKA profiles analogous to those of its matched PDX counterpart (Fig. 7A). CRC0196 and CRC0254 organoids were included as negative controls since both models did not show high INKA scores for dasatinib targets (fig. S14).

Treatment with dasatinib reduced cell viability in the micro to nano molar range in CRC0161 but not in control models CRC0196 and CRC0254 with low dasatinib target activity (Fig. 7A). In addition, the combination of low doses of both cetuximab [0,7 μg/ml (~ 5nM)] and dasatinib (5nM) impaired cell viability in CRC0161, whereas either treatment alone was ineffective (Fig. 7B). A 200-fold dose increase of the inhibitors [140 μg/ml (~ 1000nM) for cetuximab and 1000nM for dasatinib] confirmed the relatively poor responsiveness of model CRC0161 to EGFR inhibition (only approximately 40% reduction of cell viability) and its sensitivity to dasatinib (about 80% reduction). Combining cetuximab and dasatinib did not significantly reduce cell viability in CRC0161 compared to dasatinib alone, likely because monotherapy with high-dose dasatinib also blocked EGFR and was sufficient to reach the inhibitory plateau (Fig. 7B). Furthermore, as expected, treatment of CRC0161 organoids with the EGFR inhibitor afatinib as an additional control did not affect viability, confirming the finding that CRC0161 is resistant to EGFR blockade (fig. S15). Finally, JAK was chosen as another negative control since CRC0161 did not show high INKA scoring of JAK. In line with the absence of JAK target activity, treatment of CRC0161 organoids with the JAK inhibitor ruxolitinib did not reduce viability (fig. S15).

Unfortunately, CRC0161 proved unable to re-engraft in mice after thawing, which prevented in vivo validation experiments. Conversely, the other predicted dasatinib sensitive model CRC0166 was hard to grow as organoids but could be tested in vivo in a PDX assay. After three weeks of treatment, dasatinib alone was ineffective in controlling tumor growth, and cetuximab alone only retarded tumor growth. Tumors volume increased 40% on average, in agreement with our historical data in which response of this model to cetuximab was categorized as progressive disease (table 1). Conversely, the combination of dasatinib and cetuximab completely blocked tumor growth, with a significant advantage (p-value = 0.0377) in tumor volumetric reduction compared with single-agent cetuximab (Fig. 7C, Suppl. Table 11). Altogether, these experiments show that phosphoproteomics coupled to INKA analysis may provide a relevant read-out of kinase activities for individualized (combination) treatment.

DISCUSSION

This study analyzed the phospho-proteome and proteome profiles of 30 mCRC patient-derived xenografts, genomically characterized and annotated for response to cetuximab treatment, to shed light onto the signaling events associated with sensitivity and resistance to EGFR blockade in patients with mCRC. Mass spectrometry-based analysis revealed distinctive phospho-sites and proteins between cetuximab-sensitive and resistant tumors; identified kinase driver hyperactivity sustained by underlying genomics aberrations; and yielded potential kinase targets to treat genomically unexplained resistant models. The phosphoproteome and proteome provided complementary insights, and combined interpretation aided a deeper understanding of cetuximab response in mCRC tumor biology. More specifically, the tyrosine-based phosphorylation data provided insight into upstream tyrosine kinase signaling pathways more enriched in cetuximab-sensitive tumors. In contrast, the global phosphoproteome, dominated by pSer/pThr phosphosites, was enriched in downstream signaling events more associated with resistant tumors (Fig. 1). In line with our results, Rivera et al., observed positive enrichment of canonical EGFR and EGF pathway signatures in their cetuximab sensitive CRC PDX models *(20)*. Our findings support the idea that there is no single factor that can accurately predict how tumors will respond to treatment. Positive outcomes for patients are not solely determined by one factor, but rather by a combination

of multiple molecular characteristics evident in multi-omics data. Therefore, it is important to consider all factors when predicting treatment outcomes. *(19)*.

The distinctive phospho-sites and proteins combined in a network diagram, annotated with mRNA data (Fig. 2), provided more insight into the biological processes involved in cetuximab response. Sensitive tumors revealed higher phosphorylation of proteins functionally related to cell-cell contact and cellular tight junction organization, such as CXADR, CLDN1, CLDN3. Loss of junction proteins and disruption of overall cell-cell organization has historically been implicated with an early invasive and metastatic phenotype *(34)*. However, more recent studies have documented that increased expression and activity of essential proteins involved in the tight-junction organization also correlates with tumor progression, likely due to their role as signaling substrates *(35)*. For example, Pike et al. *(36)* described that CXADR potentiates EGFR signaling by delaying receptor internalization. This suggests that CXADR overexpression and phosphorylation, as observed in cetuximab-sensitive tumors, may enhance EGFR pathway activity, hence contributing to EGFR dependency. Accordingly, analysis of global gene expression data from 403 CRC PDXs for which annotation of response to cetuximab was available *(22)* revealed higher RNA expression of CXADR in cetuximab-sensitive than in cetuximab-resistant PDX models, making a solid case for CXADR as a potential predictor of response to cetuximab in metastatic colorectal cancer. Previous proteomics and phosphoproteomics analysis of acquired resistance to cetuximab in two isogenic CRC PDX models revealed multiple pathways downstream of EGFR and found endocytosis, cell-cell adhesion, tight and adherence junctions related terms enriched in the upregulated proteins and phosphosites of the sensitive model *(20)*.

GSEA revealed an association between EMT related signaling and resistance to cetuximab. EMT signaling has been previously linked to resistance to EGFR blockade (*20*) by prompting a switch to alternative kinase signaling pathways (*33*), including the AKT1 pathway. In addition, a recent study has found that CXADR acts as a negative regulator of EMT by providing an AKT-inhibitory signalosome at the tight junction (*34*). The role of CXADR as an EMT gate-keeper, combined with its ability to potentiate EGFR signaling and constrain AKT signaling, suggests that CXADR and cell-cell adhesion locks CRC cells into an epithelial phenotype dependent on EGFR-induced growth, making tumors susceptible to EGFR inhibition. Conversely, cells transitioning toward a mesenchymal phenotype become more dependent on pathways that are parallel or downstream to EGFR signaling, such as the AKT1 pathway, and are thus less vulnerable to EGFR inhibition (*18*). This assumption is consistent with our results, whereby low CXADR expression and high AKT signaling, as evidenced by both INKA and PTM-SEA analyses, typify cetuximab-resistant tumors. In a complementary perspective, activation of AKT and its downstream signaling effector mTOR has been documented to stimulate EMT (35). The relevance of AKT in cetuximab resistance is supported by the observation that AKT inhibition enhances the depth of response to cetuximab in CRC PDX models *(27)*.

OXPHOS was found to be enriched in CS tumors. Evidence that tyrosine kinase signaling can regulate mitochondrial oxidative phosphorylation function *(37)* combined with the finding that cetuximab may have a role in impairing mitochondrial function in CRC *(38)*, could suggest that tumors with a more abundant OXPHOS expression profile may be more susceptible to EGFR inhibition.

Kinase activity analysis using INKA was employed to highlight essential kinases and identified potential targets for single and combination treatment for individual tumors *(15)*. This analysis pinpointed high signaling activity of ERBB2, EGFR, and MET in resistant PDX models

in line with the corresponding gene amplifications. Moreover, INKA revealed high activity of ephrin kinases, and in particular EPHA2, in models CRC0161 and CRC0166, with genomically unexplained mechanisms of resistance. The potential of these kinases as targets was evaluated by treating organoid cultures of CRC0161 and mice harboring CRC0166 PDXs with dasatinib, a potent inhibitor of EPHA2 (low nanomolar range), several other members of the ephrin kinase family, as well SRC family kinases *(31–33)* that were also active in these models. Dasatinib is also a weak inhibitor of EGFR. When used at near-micromolar concentrations, dasatinib reduced cell viability in CRC0161 organoids compared to organoid models that did not share the high ephrin INKA profile. At low nanomolar concentrations that do not inhibit EGFR, the combination with cetuximab increased the effect of dasatinib. Likewise, mice bearing CRC0166 PDXs responded to combination therapy with cetuximab and dasatinib with disease stabilization, whereas they experienced disease progression when exposed to either monotherapy. These functional experiments show the potential of phosphoproteomics combined with INKA analysis to select a suitable treatment strategy for tumor models with previously unexplained resistance to cetuximab.

Our findings have certain limitations. For example, we have focused our analyses on the static interrogation of phosphoprotein and protein biomarkers in treatment naïve PDX tumors and correlated results with the outcome of cetuximab administration. Assessing the proteomic and signaling changes that occur over the course of therapy is expected to provide useful information about the dynamic mechanisms of tumor adaptation to antibody pressure and will contribute to identifying reactive pathways that likely compensate for target blockade. Moreover, we acknowledge that the association between resistance to cetuximab and high EPHA2 and SRC family kinase activity has not been validated in clinical samples from therapeutically annotated patients with mCRC, and thus requires further study. Regrettably, we were unable to confirm the organoid results for CRC0161 in vivo because it was unsuccessful in re-engrafting as PDX. On the other hand, although it was unable to cultivate as organoids, the projected dasatinib-sensitive model CRC0166 was viable for testing in vivo in a PDX assay.

In conclusion, this research highlights the added value of phospho-proteomics and proteomics in studying the bio-molecular basis of responses to targeted treatment in cancer. It provides insight into the biology of the primary response to treatment with cetuximab in metastatic colorectal cancer and advocates that CXADR in relation to cetuximab sensitivity deserves further study for its potential use as a biomarker for response. Additionally, this work confirmed the potential of single sample kinase activity analysis using INKA for the selection of potential treatment strategies *(15)*. Our study extends our previous analysis of the genomically unexplained resistant PDX model CRC0177 in which INSR/IGF1R activity was identified and validated as co-target for cetuximab combination treatment *(15)*. Using a down-scaled protocol that utilizes only small amounts of tumor tissues *(16)*, we recently uncovered drug-specific signatures in needle biopsies *(17)*. This underscores the feasibility of potential clinical application of pTyr phosphoproteomics. The sequential phosphopeptide capture strategy as employed here allows pTyr-phospho-proteomics to be performed together with global phosphoproteomics and proteomics on the same samples. Recent developments enable phosphoproteomics and proteomics in conjunction with other omics analyses on the same samples with further streamlining of protocols *(16, 17, 39)*. Together, these integrative approaches will further motivate the development of phosphoproteomics-based companion diagnostics for more informed patient stratification and treatment decisions, further contributing to the realization of personalized anticancer medicine.

MATERIALS AND METHODS

Study Design

This study used proteomics and phosphoproteomics to understand the biological processes that lead to sensitivity and resistance to EGFR blockade in mCRC and to identify alternative drug targets for resistant tumors. Tissue samples from 10 cetuximab-sensitive and 20 cetuximab-resistant PDXs were analyzed using label-free Liquid Chromatography with tandem mass spectrometry (LC-MS/MS) proteomics and phospho-proteomics. Biological and technical replicates of representative models were measured for reproducibility. To comprehensively investigate global phosphorylation, tyrosine-specific phosphorylation, and protein expression, pTyr-immunoprecipitation, general phosphopeptide enrichment using titanium dioxide, and global protein expression proteomics were performed in all samples. The samples were measured in 5 cohorts, and LC-MS/MS measurement reliability was assessed by including HCT116 lysates with known performance profiles in each measurement cohort. The PDX tissue samples were processed blindly, without considering molecular characteristics, and underwent histological and technical assessments as standard quality checks. Group-based statistics were performed between CS and CR tumors to find discriminative molecular determinants of response, and single-sample Integrative Inferred Kinase Activity (INKA) analysis was used to explore the potential hyperactive kinases as alternative targets. Functional validation of hyperactive kinases was performed using organoids and PDX models.

Patient-derived xenografts

Tumors were obtained from patients treated by liver metastasectomy at the Candiolo Cancer Institute (Candiolo, Torino, Italy), Mauriziano Umberto I (Torino, Italy), and San Giovanni Battista (Torino, Italy). All patients provided informed consent. Samples were procured, and the study was conducted under the approval of the Review Boards of the Institutions. The cohort studied here contains ten models sensitive to cetuximab, nine cetuximab resistant models that lack mutations in RAS or RAF genes, and 11 cetuximab resistant models that harbor a mutation in KRAS (n = 4), NRAS (n = 3) or BRAF (n = 4). Of the resistant models that lacked RAS/RAF mutations, some models did harbor a genomic aberration relevant to cetuximab resistance, including 2 models with an amplification of ERBB2, 1 model with an amplification of MET,1 model with a mutation in ERBB2 (V777L), 1 model with a mutation in MAP2K1 (K57N) and 1 model with a mutation in EGFR (G465R) (Suppl. Table 1). For a subset of model's representative of the whole cohort in this study, biological and or technical replicates were available to assess reproducibility (Suppl. Table 1). In addition, representative tumor slices were assessed by pathology for percentage tumor, stromal tissue, and necrosis. Pathology report was not used as an upfront exclusion criterion for analysis.

Organoid cultures and cell viability

Organoids were established from colorectal cancer patient-derived xenografts CRC0161, CRC0196 and CRC0254 and cultured in extracellular matrix hydrogel (Cultrex pathClear, Reduced Growth Factor Basement Membrane Extract, type 2) and Dulbecco's Modified Eagle's Medium (DMEM) F12 culture medium supplemented with 1% penicillin/streptomycin, 1% B27, 1% N2, 2 mM L-glutamine, 1nM N-acetyl-cysteine and 0.02 µg/ml EGF. For testing viability, organoids were seeded as single cells on a coating of BME hydrogel in the above culture medium depleted of EGF growth factor. After seven days, CellTiter-Glo luminescent cell viability assay (Promega) was used, as described before *(40)*, to measure viability. Results were analyzed using

PRISM GraphPad software and statistical analysis was performed using ordinary one-way ANOVA. Error bars were calculated based on SEM.

In vivo treatments

Tumor implantation and expansion were performed as previously described *(41)*. Briefly, tumor material not required for histopathologic analysis was collected and placed in medium 199 supplemented with 200 U/mL penicillin, 200 µg/mL streptomycin, and 100 µg/mL levofloxacin. Each sample was cut into 25- to 30-mm^3 pieces in antibiotic-containing medium; some of the pieces were snap-frozen in liquid nitrogen for phospho-proteomics, and some others were incubated overnight in RNAlater and then frozen at −80°C for DNA and RNA analyses; 2 other pieces were coated in Matrigel (BD Biosciences) and implanted in 2 different 4- to 6-week-old male or female NOD (nonobese diabetic)/SCID (severe combined immunodeficient) mice. After mass formation, the tumors were passaged and expanded for 2 generations until production of a cohort of 12 or 24 mice, depending on the amount of the original material. Established tumors (average volume 400 mm^3) were treated for three weeks with the following regimens, either single-agent or in combination: cetuximab (Merck) 20 mg/kg by intraperitoneal injection, twice-weekly (vehicle: physiological saline); dasatinib (Carbosynth) 50 mg/kg, daily by oral gavage (vehicle: 80 mM sodium citrate, pH 3.1). Tumor size was evaluated once- weekly by caliper measurements and the approximate volume of the mass was calculated using the formula $4/3\pi\cdot(d/2)2\cdot D/2$, where d is the minor tumor axis and D is the major tumor axis. For assessment of tumor response to therapy, we adopted a classification loosely inspired by clinical criteria *(9, 10, 16, 27)*: (i) tumor regression was defined as a decrease of at least 50% in the volume of target lesions, taking as reference the baseline tumor volume; (ii) at least a 35% increase in tumor volume was categorized as disease progression; and (iii) responses that were neither sufficient reduction to qualify for shrinkage nor sufficient increase to qualify for progression were considered as disease stabilization. Animal procedures were approved by the Italian Ministry of Health (authorization 806/2016-PR).

Tissue lysis and phosphopeptide enrichment

Tissue from patient-derived xenograft was cut on a cryotome in 20µM slices and lysed in lysis buffer (9 M urea, 20 mM 4-(2-hydroxyethyl)-1-piperazineethanesulfonic acid (HEPES) pH 8.0, 1 mM sodium orthovanadate, 2.5 mM sodium pyrophosphate, 1mM ß-glycerophosphate) in a 1:40 wet-weight to lysis buffer ratio, sonicated (3 cycles of 30 s) and extracts were stored at -80 ºC.

For phosphoproteomics, lysate aliquots equivalent to 5.5 mg total protein were used as described before *(42, 43)*. Proteins were reduced by incubation in 4.5 mM dithiothreitol for 30 min at 55 ºC, alkylated in 10 mM iodoacetamide for 15 min at room temperature in the dark, and digested overnight at room temperature with 10 µg/ml trypsin after fourfold dilution with 20 mM HEPES pH 8.0, to reduce the urea concentration. After acidification (trifluoroacetic acid to 1% final concentration), tryptic digests were desalted on Sep-Pak C18 cartridges (Waters Chromatography), divided in aliquots for immunoprecipitation (5mg) or affinity enrichment (500µg) and lyophilized and stored at -80 ºC.

For immunoprecipitation of tyrosine-phosphorylated peptides, peptides were dissolved in 350 µl immunoprecipitation buffer (50 mM 3-(N-morpholino)propanesulfonic acid (MOPS) pH 7.2, 10 mM sodium phosphate, 50 mM NaCl) and transferred at 4 ºC to a microcentrifuge tube containing 20 µl of a 50% (v/v) slurry of agarose beads harboring P-Tyr-1000 anti-phosphotyrosine monoclonal antibodies (Cell Signaling Technologies) that had been washed and

taken up in PBS. After 2-h of incubation at 4 ºC on a head-over-tail rotator, beads were washed twice with cold PBS and three times with cold High-performance liquid chromatography (HPLC) grade water. Bound peptides were eluted with a total of 50 µl 0.15% trifluoroacetic acid in two steps. Phosphopeptides were desalted using 200 µl STAGE tips containing a 16G empore SDB-XC membrane plug (3 M) using the same solvents as used for the Seppak cartridge (20 µl, 1000 ×g, 1 min). Desalted peptides were dried in a vacuum centrifuged at 45°C and solubilized in 20 µl 4% acetonitrile/0.5% trifluoroacetic acid, prior to LC-MS/MS analysis on the same day.

For global affinity enrichment of phosphopeptides, aliphatic hydroxy-acid modified metal oxide chromatography using TiO_2 beads was performed *(44)*. Briefly, 500 µg peptides (1 µg/µl) were mixed with 500 µl washing buffer (80% ACN, 0.1%TFA containing 300 mg/ml lactic acid) and applied to 2.5 mg TiO_2 beads (GL sciences, 10 µm) packed in a 200 µl STAGE tip containing a 16G empore C8 membrane plug (3 M, St Paul, MN). The STAGE tip was washed with 200 µl washing buffer, followed by 200 µl of 80% ACN and 0.1% TFA. Phosphopeptides were eluted in two steps in 50 µl 0.5% and 5% piperidine (Fisher Scientific) and were quenched in 100 µl 20% H_3PO_4. All steps were performed by centrifugation (1500 ×g, 4 min). Phosphopeptides were desalted using SDB-XC STAGE tips as described above. Desalted phosphopeptides were dried in a vacuum centrifuge and redissolved in 30 µl 4%ACN, 0.5%TFA;15 µl was injected on column

Protein-expression profiling

Protein lysates (50 µg) were separated on precast 4–12% gradient gels using the NuPAGE SDS-PAGE system (Invitrogen, Carlsbad, CA). Following electrophoresis, gels were fixed in 50% ethanol/3% phosphoric acid solution and stained with Coomassie R-250. Gel lanes were cut into five bands, and each band was cut into ~1 mm3 cubes. Gel cubes were washed with 50 mM ammonium bicarbonate/50% acetonitrile and were transferred to a 1.5 ml microcentrifuge tube, vortexed in 400 µl 50 mM ammonium bicarbonate for 10 min, and pelleted. The supernatant was removed, and the gel cubes were vortexed in 400 µl 50 mM ammonium bicarbonate/50% acetonitrile for 10 min. After pelleting and removal of the supernatant, this wash step was repeated. Subsequently, gel cubes were reduced in 50 mM ammonium bicarbonate supplemented with 10 mM DTT at 56°C for 1 h. The supernatant was removed, and gel cubes were alkylated in 50 mM ammonium bicarbonate supplemented with 50 mM iodoacetamide for 45 min at room temperature in the dark. Next, gel cubes were washed with 50 mM ammonium bicarbonate/50% acetonitrile dried in a vacuum centrifuge at 50°C for 10 min and covered with trypsin solution (6.25 ng/µl in 50 mM ammonium bicarbonate). Following rehydration with trypsin solution and removing excess trypsin, gel cubes were covered with 50 mM ammonium bicarbonate and incubated overnight at 25°C. Peptides were extracted from the gel cubes with 100 µl of 1% formic acid (once) and 100 µl of 5% formic acid/50% acetonitrile (twice). For each sample the three extracts were pooled and stored at −20°C until use. Before LC-MS, the extracts were concentrated in a vacuum centrifuge at 50°C, and volumes were adjusted to 50 µl by adding 0.05% formic acid, filtered through a 0.45 um spin filter, and transferred to an LC autosampler vial.

LC-MS/MS

Peptides were separated on an Ultimate 3000 nanoLC-MS/MS system (Dionex LC-Packings) equipped with a 20-cm, 75-µm inner diameter fused silica column custom packed with 1.9-µm ReproSil-Pur C18-AQ silica beads (120-Å pore size; Dr. Maisch). After injection, peptides were trapped at 6 µl/min on a 10-mm, 100-µm inner diameter trap column packed with 5-µm ReproSil-Pur C18-AQ silica beads (120-Å pore size) in buffer A (buffer A: 0.5% acetic acid, buffer B: 80%

acetonitrile, 0.5% acetic acid), and separated at 300 ml/min with a 10–40% buffer B gradient in 90 min (120 min inject-to-inject). Eluting peptides were ionized at a potential of +2 kV and introduced into a Q Exactive mass spectrometer (Thermo Fisher). Intact masses were measured in the orbitrap with a resolution of 70,000 (at m/z 200) using an automatic gain control (AGC) target value of 3×10^6 charges. Peptides with the top 10 highest signals (charge states 2+ and higher) were submitted to MS/MS in the higher-energy collision cell (4-Da isolation width, 25% normalized collision energy). MS/MS spectra were acquired in the orbitrap with a resolution of 17,500 (at m/z 200) using an AGC target value of 2×10^5 charges and an underfill ratio of 0.1%. Dynamic exclusion was applied with a repeat count of 1 and an exclusion time of 30 s.

Peptide identification

MS/MS spectra of both phosphopeptide enrichment experiments (TiO_2 and pTyr IP) were searched against the UniProt human reference proteome FASTA file (downloaded August 2015, no fragments; 62447 entries entries) using MaxQuant 1.5.2.8 software. To cross-check the phosphoproteome results from the database search against the human genome, we also searched the phosphoproteomics data against the same combined human and mouse sequences as we did for the proteome expression dataset. MS/MS spectra of the protein expression experiment were searched against the same human FASTA file and the Uniprot mouse reference FASTA file (downloaded June 2015, no fragments, canonical and isoforms; 42296 entries) Enzyme specificity was set to trypsin, and up to two missed cleavages were allowed. Cysteine carboxamidomethylation (+57.021464 Da) was treated as fixed modification and serine, threonine, and tyrosine phosphorylation (+79.966330 Da), methionine oxidation (+15.994915 Da), and N-terminal acetylation (+42.010565 Da) as variable modifications. Peptide precursor ions were searched with a maximum mass deviation of 4.5 ppm and fragment ions with a maximum mass deviation of 20 ppm. Peptide and protein identifications were filtered at a false discovery rate of 1% using a decoy database strategy. The minimal peptide length was set at 7 amino acids, the minimum Andromeda score for modified peptides was 40, and the corresponding minimum delta score was 6. Proteins that could not be differentiated based on MS/MS spectra alone were clustered into protein groups (default MaxQuant settings). Phosphopeptide identifications were propagated across samples using the 'match between runs' option checked. In the protein expression search match between runs was not applied. Phosphopeptide MS/MS spectral counts were calculated from the MaxQuant evidence file using R.

Organoid phosphoproteomics

For organoids phosphoproteomics, lysate aliquots (1.6 mg total protein) were reduced, alkylated, digested, and desalted as described. For pTyr immunoprecipitation, peptides were dissolved in 350 µl IP buffer with 20 µl 50% (v/v) P-Tyr-1000 agarose beads and pTyr phosphopeptides were captured and desalted as described. The non-bound fraction was desalted as well and TiO2 beads were used for pSer/pThr phosphopeptide enrichment as described, using 500 µg peptides as input. For protein-expression profiling 1 µg of the non-bound fraction of the pTyr IP was used for single-shot analysis. Peptides were separated on an Ultimate 3000 nanoLC-MS/MS system (Dionex LC-Packings) equipped with a 50-cm 75 µm ID C18 Acclaim pepmap column (Thermo Scientific). After injection, peptides were trapped at 3 µl/min on a 10-mm, 75-µm ID Acclaim Pepmap trap column (Thermo Scientific) in buffer A (buffer A: 0.1% formic acid, buffer B: 80% acetonitrile, 0.1% formic acid), and separated at 300 ml/min with a 10–40% buffer B gradient in 90 min (120 min inject-to-inject). Eluting peptides were ionized at a potential of +2 kV and introduced into a Q Exactive HF mass spectrometer (Thermo Fisher). Intact masses were measured in the orbitrap

with a resolution of 120,000 (at m/z 200) using an automatic gain control (AGC) target value of 3 × 10^6 charges. Peptides with the top 15 highest signals (charge states 2+ and higher) were submitted to MS/MS in the higher-energy collision cell (1.6-Da isolation width, 25% normalized collision energy). MS/MS spectra were acquired in the Orbitrap with a resolution of 15.000 (at m/z 200) using an AGC target value of 2 × 10^5 charges and an under fill ratio of 0.1%. Dynamic exclusion was applied with a repeat count of 1 and an exclusion time of 30 s.

MS/MS spectra of both phosphopeptide enrichment experiments (TiO2 and pTyr IP) were searched against the Swissprot human_canonical_and_isoform.fasta (42258 entries)t FASTA file (downloaded January 2018, canonical and isoforms; 42258 entries) using MaxQuant 1.6.0.16. Search setting were the same as described for PDX models. Proteins that could not be differentiated based on MS/MS spectra alone were clustered into protein groups (default MaxQuant settings). Phosphopeptide identifications were propagated across samples using the 'match between runs' option checked. Phosphopeptide MS/MS spectral counts were calculated from the MaxQuant evidence file using R. For phosphopeptide data, we used data from the MaxQuant 'modificationSpecificPeptides' table. For phosphosite data, we used data from the MaxQuant' Phospho (STY) Sites' table.

Quantification

Group-based comparisons were made with MS/MS spectral counts for protein expression data and MS ion intensities (area under the MS1 extracted ion chromatogram) for the phosphosite data. Moreover, INKA uses spectral counts as input.

Data filtering and annotation.

For phosphopeptide data, we used data from the MaxQuant 'modificationSpecificPeptides' table. Table rows with data linked to multiple UniProt gene symbols were deconvoluted into separate rows with a single gene symbol. For phosphosite data, we used data from the MaxQuant' Phospho (STY) Sites' table, filtering for so-called class I sites (localization probability > 0.75). Table rows with data linked to multiple UniProt accessions, and those linked to multiple phosphopeptides, were deconvoluted into separate rows. Data from the web resources UniProt (UniProt Consortium, 2015) (for mapping attributes of UniProt accessions; www.uniprot.org, mapping date 8 June 2016), PhosphoSitePlus *(45)* (for experimentally observed phosphorylation sites and kinase-substrate relationships; www.phosphosite.org, Phosphorylation_site_dataset, and Kinase_Substrate_Dataset, versions of 3 July 2016) and KinBase *(46)* (for currently recognized protein kinases; kinase.com/web/current/kinbase, mapping date 20 July 2016), and HGNC *(47)* (for mapping to official gene symbols of the HUGO Gene Nomenclature Committee; www.genenames.org) were used in combination with a UniProt human reference proteome FASTA file derived from release 2014_01 filtered for "no fragments," and containing 21849 TrEMBL entries and 39703 Swiss-Prot entries to prioritize rows linking the same phosphosite to the same gene, only retaining the row with the best-annotated accession. Subsequently, the phosphosite data were merged with pertinent phosphopeptide data in a single, non-redundant class-I phosphosite-phosphopeptide table.

2-group comparisons

Group comparisons were made between all cetuximab sensitive and all resistant models (CS vs. CR-ALL), between sensitive and resistant models lacking mutations in RAS/RAF (CS vs. CR-WT), and between sensitive (CS-WT) and resistant RAS/RAF mutant models (CS vs. CR-MUT).

For phospho-proteomics data, phosphosite intensities were taken from the non-redundant class-I phosphosite-phosphopeptide table and normalized using the sum of all intensities and median centering of the values in each sample. Biological and technical replicates were averaged omitting zero values from average and missing data points were imputed using the half-min method. Limma was then performed for each group comparison using the R package "limma" *(48)*. Nominal p-values were not corrected for multiple tests. Results of each group comparison were filtered for p-value (< 0.01), fold change (< -1.5, > 1.5), average intensity (> $1*10^7$), and data coverage of more than 50% in at least one of the comparison groups. Analysis was performed separately for data derived from pTyr-immunoprecipitation and TiO2 affinity capture. For global protein expression, protein spectral counts were normalized, and biological and technical replicates were averaged, omitting zero values from average. A beta-binomial test was then performed for each group comparison using the R package "ibb" as described before *(49)*. Nominal p-values were not corrected for multiple tests. Results of each group comparison were filtered for p-value (< 0.01), fold change (< -1.5, > 1.5), and data coverage of more than 50% in at least one of the comparison groups. Heatmaps were created with the R package ComplexHeatmap *(50)* utilizing z-score normalization, euclidean distance, and ward.D2 linkage.

RNA expression data was analyzed where RNAsub refers to a comparison among the same subset of PDX models also used for (phospho-)proteomics profiling, and RNA400 refers to a comparison among an extensive collection of 157 CS and 246 CR models. Gene probes were kept if considered expressed in Isella et al. (2017) *(22)* or excluded if probes cross-reacted with murine genes. When there were multiple probes per gene, only the probe with the highest standard deviation was picked. Two-group comparisons were made between CS vs. CR-ALL, CS vs. CR-WT, and CS vs. CR-MUT using limma *(48)* on log2-scaled expression values. Nominal p-values were corrected for multiple tests using the Benjamini & Hochberg procedure *(51)*. For the RNAsub comparison, no RNA-sequencing data was available for 9 CR-MUT models. In addition, model CRC0358 (CR-WT) was not considered for RNA analyses due to outlier behavior. The CS vs. CR-MUT comparison on RNA level was excluded because it was unbalanced and underpowered.

Expression-driven signature enrichment analysis

Gene set enrichment analysis (GSEA) was conducted using the "fgsea" R package *(52)*. The analysis utilized ranked genes, including log-transformed and signed p-values obtained from protein expression comparisons between CS and CR, as well as RNA400 CS versus CR-all. The C5 ontology gene sets collection from the MSigDB v7.2 database served as input files. The resulting GSEA outputs were visualized in R, employing the ggplot2 package *(53)*.

Post-translational modification signature enrichment analysis

Phosphosite-specific signature analysis was performed with post-translational modification signature enrichment analysis (PTM-SEA) *(54)* using the R-script ssgsea-gui.R (https://github.com/broadinstitute/ssGSEA2.0). Ranked phosphosites (log-transformed and signed p-values of the CS vs. CR comparisons) and the PTMsigDB v1.9.0 database was used as input files. Visualization of results was performed in R using the ggplot2 package *(53)*.

Overlap analysis

Using Venny 2.1.0 *(55)*, the overlap of significant phospho-sites and proteins of the comparisons CS vs. CR-ALL, CR-MUT, and CR-WT created three response signatures. The general response signature consisted of significant phospho-sites and proteins exclusive in the comparison of CS

vs. CR-ALL (Venn part CR1 and CS1) combined with the overlap of all comparisons (Venn part CR2 and CS2) and the overlap between CS vs. CR-MUT and CR-WT (Venn part CR3 and CS3). The signatures for either RAS/RAF mutated or wild-type tumors contained significant phospho-sites and proteins exclusive to CS vs. CR-MUT (Venn part CR4 and CS4) or CS vs. CR-WT (Venn part CR5 and CS5). The significant phospho-sites and proteins of the overlap between CS vs. CR-ALL and CS vs. CR-MUT or CS vs. CR-WT were excluded. These significant phospho-sites and proteins could not be qualified as a general response or specific for RAS/RAF mutated or wild-type tumors.

Analysis of biological pathways and processes

Phospho-sites and proteins from the general response signature, RAS/RAF mutated signature, and the wild-type signature were combined in one table (179 proteins and 83 phosphosites). All (phospho)proteins were used to retrieve protein-protein association data from the STRING database v11 *(56)* to build a combined network in Cytoscape v3.7 *(57)*. Statistical data encompassed three comparisons: CS vs. CR-ALL, CR-MUT, and CR-WT. The maximum fold change among these three comparisons was log2-transformed and used to color-code a donut ring around the pertinent network node for every protein or phosphosite. Using the Cytoscape Omics Visualizer app *(58)*, a separate donut ring was added for expression, pTyrIP, or TiOx.

To complement the protein data, we also analyzed RNAseq data on the models in the present cohort (RNAsub) as well as on a larger cohort of 157 cetuximab sensitive and 246 cetuximab resistant PDX tumors (RNA400) *(22)*. RNA features were tested in the three comparisons mentioned above using the limma R package and filtered for a link to the (phospho)proteins in the network. If any of the comparisons were significant ($p < 0.05$), the associated network node was colored orange or blue, depending on the direction of change in the CS vs. CR-ALL comparisons.

Protein clusters were identified using the MCL algorithm of the clusterMaker2 app *(59)* inside Cytoscape, and gene ontology analysis was performed with the BiNGO app *(60)* using ontology definitions of April 2020 to analyze biology covered in this network.

INKA analysis

Integrative Inferred Kinase Activity (INKA) based on both phosphorylated kinases and their substrates was calculated for each sample as previously described *(15)*. Mean INKA scores for CS and CR tumors were calculated for each kinase, excluding kinases measured in less than five tumors.

Statistics

Statistical analysis was conducted on the phosphosite intensities by normalizing them using the sum of all intensities and median centering within each sample. Averages of biological and technical replicates were calculated, excluding zero values, and missing data points were imputed using the half-min method. Group comparisons for phosphosite intensities were performed using the R package "limma," nominal p-values were obtained without correction for multiple tests. The R package "ibb" was utilized with a beta-binomial test for group comparisons of global protein expression. Furthermore, statistical analyses for organoid viability assays were carried out in Prism 7.0 software (GraphPad) using ordinary one-way ANOVA. Statistical significance was determined for all experiments using the following criteria: n.s. (not significant), $*p < 0.05$, $**p < 0.01$, $***p < 0.001$.

Supplementary Materials

fig. S1. to S14.

Table S1. to S11

Data file S1

MDAR reproducibility checklist

References

1. J. R. Hecht, A. Cohn, S. Dakhil, M. Saleh, B. Piperdi, M. Cline-Burkhardt, Y. Tian, W. Y. Go, SPIRITT: A Randomized, Multicenter, Phase II Study of Panitumumab with FOLFIRI and Bevacizumab with FOLFIRI as Second-Line Treatment in Patients with Unresectable Wild Type KRAS Metastatic Colorectal Cancer, *Clin. Colorectal Cancer* **14**, 72–80 (2015).

2. L. S. Schwartzberg, F. Rivera, M. Karthaus, G. Fasola, J.-L. Canon, J. R. Hecht, H. Yu, K. S. Oliner, W. Y. Go, PEAK: A Randomized, Multicenter Phase II Study of Panitumumab Plus Modified Fluorouracil, Leucovorin, and Oxaliplatin (mFOLFOX6) or Bevacizumab Plus mFOLFOX6 in Patients With Previously Untreated, Unresectable, Wild-Type KRAS Exon 2 Metastatic Colorectal , *J. Clin. Oncol.* **32**, 2240–2247 (2014).

3. V. Heinemann, L. F. von Weikersthal, T. Decker, A. Kiani, U. Vehling-Kaiser, S.-E. Al-Batran, T. Heintges, C. Lerchenmüller, C. Kahl, G. Seipelt, F. Kullmann, M. Stauch, W. Scheithauer, J. Hielscher, M. Scholz, S. Müller, H. Link, N. Niederle, A. Rost, H.-G. Höffkes, M. Moehler, R. U. Lindig, D. P. Modest, L. Rossius, T. Kirchner, A. Jung, S. Stintzing, FOLFIRI plus cetuximab versus FOLFIRI plus bevacizumab as first-line treatment for patients with metastatic colorectal cancer (FIRE-3): a randomised, open-label, phase 3 trial, *Lancet Oncol.* **15**, 1065–1075 (2014).

4. E. J. van Helden, C. W. Menke-van der Houven van Oordt, M. W. Heymans, J. C. F. Ket, R. van den Oord, H. M. W. Verheul, Optimal use of anti-EGFR monoclonal antibodies for patients with advanced colorectal cancer: a meta-analysis, *Cancer Metastasis Rev.* **36**, 395–406 (2017).

5. A. B. Benson, A. P. Venook, L. Cederquist, E. Chan, Y.-J. Chen, H. S. Cooper, D. Deming, P. F. Engstrom, P. C. Enzinger, A. Fichera, J. L. Grem, A. Grothey, H. S. Hochster, S. Hoffe, S. Hunt, A. Kamel, N. Kirilcuk, S. Krishnamurthi, W. A. Messersmith, M. F. Mulcahy, J. D. Murphy, S. Nurkin, L. Saltz, S. Sharma, D. Shibata, J. M. Skibber, C. T. Sofocleous, E. M. Stoffel, E. Stotsky-Himelfarb, C. G. Willett, C. S. Wu, K. M. Gregory, D. Freedman-Cass, Colon Cancer, Version 1.2017, NCCN Clinical Practice Guidelines in Oncology, *J. Natl. Compr. Cancer Netw.* **15**, 370–398 (2017).

6. E. Van Cutsem, A. Cervantes, R. Adam, A. Sobrero, J. H. Van Krieken, D. Aderka, E. Aranda Aguilar, A. Bardelli, A. Benson, G. Bodoky, F. Ciardiello, A. D'Hoore, E. Diaz-Rubio, J.-Y. Douillard, M. Ducreux, A. Falcone, A. Grothey, T. Gruenberger, K. Haustermans, V. Heinemann, P. Hoff, C.-H. Köhne, R. Labianca, P. Laurent-Puig, B. Ma, T. Maughan, K. Muro, N. Normanno, P. Österlund, W. J. G. Oyen, D. Papamichael, G. Pentheroudakis, P. Pfeiffer, T. J. Price, C. Punt, J. Ricke, A. Roth, R. Salazar, W. Scheithauer, H. J. Schmoll, J. Tabernero, J. Taïeb, S. Tejpar, H. Wasan, T. Yoshino, A. Zaanan, D. Arnold, ESMO consensus guidelines for the management of patients with metastatic colorectal cancer, *Ann. Oncol.* **27**, 1386–1422

(2016).

7. T. J. Price, M. Peeters, T. W. Kim, J. Li, S. Cascinu, P. Ruff, A. S. Suresh, A. Thomas, S. Tjulandin, K. Zhang, S. Murugappan, R. Sidhu, Panitumumab versus cetuximab in patients with chemotherapy-refractory wild-type KRAS exon 2 metastatic colorectal cancer (ASPECCT): a randomised, multicentre, open-label, non-inferiority phase 3 study, *Lancet Oncol.* **15**, 569–579 (2014).

8. D. Arnold, B. Lueza, J.-Y. Douillard, M. Peeters, H.-J. Lenz, A. Venook, V. Heinemann, E. Van Cutsem, J.-P. Pignon, J. Tabernero, A. Cervantes, F. Ciardiello, Prognostic and predictive value of primary tumour side in patients with RAS wild-type metastatic colorectal cancer treated with chemotherapy and EGFR directed antibodies in six randomized trials, *Ann. Oncol.* **28**, 1713–1729 (2017).

9. A. Bertotti, G. Migliardi, F. Galimi, F. Sassi, D. Torti, C. Isella, D. Corà, F. Di Nicolantonio, M. Buscarino, C. Petti, D. Ribero, N. Russolillo, A. Muratore, P. Massucco, A. Pisacane, L. Molinaro, E. Valtorta, A. Sartore-Bianchi, M. Risio, L. Capussotti, M. Gambacorta, S. Siena, E. Medico, A. Sapino, S. Marsoni, P. M. Comoglio, A. Bardelli, L. Trusolino, D. Cora, F. Di Nicolantonio, M. Buscarino, C. Petti, D. Ribero, N. Russolillo, A. Muratore, P. Massucco, A. Pisacane, L. Molinaro, E. Valtorta, A. Sartore-Bianchi, M. Risio, L. Capussotti, M. Gambacorta, S. Siena, E. Medico, A. Sapino, S. Marsoni, P. M. Comoglio, A. Bardelli, L. Trusolino, A Molecularly Annotated Platform of Patient-Derived Xenografts ("Xenopatients") Identifies HER2 as an Effective Therapeutic Target in Cetuximab-Resistant Colorectal Cancer, *Cancer Discov.* **1**, 508–523 (2011).

10. A. Bertotti, E. Papp, S. Jones, V. Adleff, V. Anagnostou, B. Lupo, M. Sausen, J. Phallen, C. a. Hruban, C. Tokheim, N. Niknafs, M. Nesselbush, K. Lytle, F. Sassi, F. Cottino, G. Migliardi, E. R. Zanella, D. Ribero, N. Russolillo, A. Mellano, A. Muratore, G. Paraluppi, M. Salizzoni, S. Marsoni, M. Kragh, J. Lantto, A. Cassingena, Q. K. Li, R. Karchin, R. Scharpf, A. Sartore-Bianchi, S. Siena, L. a. Diaz, L. Trusolino, V. E. Velculescu, The genomic landscape of response to EGFR blockade in colorectal cancer, *Nature* **526**, 263–267 (2015).

11. S. M. Kavuri, N. Jain, F. Galimi, F. Cottino, S. M. Leto, G. Migliardi, A. C. Searleman, W. Shen, J. Monsey, L. Trusolino, S. A. Jacobs, A. Bertotti, R. Bose, HER2 Activating Mutations Are Targets for Colorectal Cancer Treatment, *Cancer Discov.* **5**, 832–841 (2015).

12. M. A. Lemmon, J. Schlessinger, Cell Signaling by Receptor Tyrosine Kinases, *Cell* **141**, 1117–1134 (2010).

13. C. R. Jimenez, H. M. W. Verheul, Mass Spectrometry-Based Proteomics: From Cancer Biology to Protein Biomarkers, Drug Targets, and Clinical Applications, *Am. Soc. Clin. Oncol. Educ. B.* , e504–e510 (2014).

14. P. Casado, M. Hijazi, D. Britton, P. R. Cutillas, Impact of phosphoproteomics in the translation of kinase-targeted therapies, *Proteomics* **17**, 1600235 (2017).

15. R. Beekhof, C. Alphen, A. A. Henneman, J. C. Knol, T. V Pham, F. Rolfs, M. Labots, E. Henneberry, T. Y. Le Large, R. R. Haas, S. R. Piersma, V. Vurchio, A. Bertotti, L. Trusolino, H. M. Verheul, C. R. Jimenez, INKA, an integrative data analysis pipeline for phosphoproteomic inference of active kinases, *Mol. Syst. Biol.* **15**, 1–22 (2019).

16. M. Labots, J. C. van der Mijn, R. Beekhof, S. R. Piersma, R. R. de Goeij-de Haas, T. V.

Pham, J. C. Knol, H. Dekker, N. C. T. van Grieken, H. M. W. Verheul, C. R. Jiménez, Phosphotyrosine-based-phosphoproteomics scaled-down to biopsy level for analysis of individual tumor biology and treatment selection, *J. Proteomics* **162**, 99–107 (2017).

17. M. Labots, T. V. Pham, R. J. Honeywell, J. C. Knol, R. Beekhof, R. de Goeij-de Haas, H. Dekker, M. Neerincx, S. R. Piersma, J. C. van der Mijn, D. L. van der Peet, M. R. Meijerink, G. J. Peters, N. C. T. van Grieken, C. R. Jiménez, H. M. W. Verheul, Kinase Inhibitor Treatment of Patients with Advanced Cancer Results in High Tumor Drug Concentrations and in Specific Alterations of the Tumor Phosphoproteome, *Cancers (Basel).* **12**, 330 (2020).

18. S. Vasaikar, C. Huang, X. Wang, V. A. Petyuk, S. R. Savage, B. Wen, Y. Dou, Y. Zhang, Z. Shi, O. A. Arshad, M. A. Gritsenko, L. J. Zimmerman, J. E. McDermott, T. R. Clauss, R. J. Moore, R. Zhao, M. E. Monroe, Y.-T. Wang, M. C. Chambers, R. J. C. Slebos, K. S. Lau, Q. Mo, L. Ding, M. Ellis, M. Thiagarajan, C. R. Kinsinger, H. Rodriguez, R. D. Smith, K. D. Rodland, D. C. Liebler, T. Liu, B. Zhang, A. Pandey, A. Paulovich, A. Hoofnagle, D. R. Mani, D. W. Chan, D. F. Ransohoff, D. Fenyo, D. L. Tabb, D. A. Levine, E. S. Boja, E. Kuhn, F. M. White, G. A. Whiteley, H. Zhu, H. Zhang, I.-M. Shih, J. Bavarva, J. Whiteaker, K. A. Ketchum, K. R. Clauser, K. Ruggles, K. Elburn, L. Hannick, M. Watson, M. Oberti, M. Mesri, M. E. Sanders, M. Borucki, M. A. Gillette, M. Snyder, N. J. Edwards, N. Vatanian, P. A. Rudnick, P. B. McGarvey, P. Mertins, R. R. Townsend, R. R. Thangudu, R. C. Rivers, S. H. Payne, S. R. Davies, S. Cai, S. E. Stein, S. A. Carr, S. J. Skates, S. Madhavan, T. Hiltke, X. Chen, Y. Zhao, Y. Wang, Z. Zhang, Proteogenomic Analysis of Human Colon Cancer Reveals New Therapeutic Opportunities, *Cell* **177**, 1035-1049.e19 (2019).

19. C. Li, Y. Di Sun, G. Y. Yu, J. R. Cui, Z. Lou, H. Zhang, Y. Huang, C. G. Bai, L. L. Deng, P. Liu, K. Zheng, Y. H. Wang, Q. Q. Wang, Q. R. Li, Q. Q. Wu, Q. Liu, Y. Shyr, Y. X. Li, L. N. Chen, J. R. Wu, W. Zhang, R. Zeng, Integrated Omics of Metastatic Colorectal Cancer, *Cancer Cell* **38**, 734-747.e9 (2020).

20. M. Rivera, I. Fichtner, A. Wulf-Goldenberg, C. Sers, J. Merk, G. Patone, K. M. Alp, T. Kanashova, P. Mertins, J. Hoffmann, U. Stein, W. Walther, Patient-derived xenograft (PDX) models of colorectal carcinoma (CRC) as a platform for chemosensitivity and biomarker analysis in personalized medicine, *Neoplasia (United States)* **23**, 21–35 (2021).

21. E. R. Zanella, F. Galimi, F. Sassi, G. Migliardi, F. Cottino, S. M. Leto, B. Lupo, J. Erriquez, C. Isella, P. M. Comoglio, E. Medico, S. Tejpar, E. Budinská, L. Trusolino, A. Bertotti, IGF2 is an actionable target that identifies a distinct subpopulation of colorectal cancer patients with marginal response to anti-EGFR therapies, *Sci. Transl. Med.* **7**, 272ra12 (2015).

22. C. Isella, F. Brundu, S. E. Bellomo, F. Galimi, E. Zanella, R. Porporato, C. Petti, A. Fiori, F. Orzan, R. Senetta, C. Boccaccio, E. Ficarra, L. Marchionni, L. Trusolino, E. Medico, A. Bertotti, Selective analysis of cancer-cell intrinsic transcriptional traits defines novel clinically relevant subtypes of colorectal cancer, *Nat. Commun.* **8**, 15107 (2017).

23. B. Zhao, L. Wang, H. Qiu, M. Zhang, L. Sun, P. Peng, Q. Yu, X. Yuan, Mechanisms of resistance to anti-EGFR therapy in colorectal cancer, *Oncotarget* **8**, 3980–4000 (2017).

24. Y.-Z. Liu, H. Yang, J. Cao, Y.-Y. Jiang, J.-J. Hao, X. Xu, Y. Cai, M.-R. Wang, KIAA1522 is a novel prognostic biomarker in patients with non-small cell lung cancer, *Sci. Rep.* **6**, 24786 (2016).

25. A. Bardelli, S. Corso, A. Bertotti, S. Hobor, E. Valtorta, G. Siravegna, A. Sartore-Bianchi, E.

Scala, A. Cassingena, D. Zecchin, M. Apicella, G. Migliardi, F. Galimi, C. Lauricella, C. Zanon, T. Perera, S. Veronese, G. Corti, A. Amatu, M. Gambacorta, L. a Diaz, M. Sausen, V. E. Velculescu, P. Comoglio, L. Trusolino, F. Di Nicolantonio, S. Giordano, S. Siena, Amplification of the MET Receptor Drives Resistance to Anti-EGFR Therapies in Colorectal Cancer, *Cancer Discov.* **3**, 658–673 (2013).

26. S. M. Leto, F. Sassi, I. Catalano, V. Torri, G. Migliardi, E. R. Zanella, M. Throsby, A. Bertotti, L. Trusolino, Sustained Inhibition of HER3 and EGFR Is Necessary to Induce Regression of HER2 -Amplified Gastrointestinal Carcinomas, *Clin. Cancer Res.* **21**, 5519–5531 (2015).

27. B. Lupo, F. Sassi, M. Pinnelli, F. Galimi, E. R. Zanella, V. Vurchio, G. Migliardi, P. A. Gagliardi, A. Puliafito, D. Manganaro, P. Luraghi, M. Kragh, M. W. Pedersen, I. D. Horak, C. Boccaccio, E. Medico, L. Primo, D. Nichol, I. Spiteri, T. Heide, A. Vatsiou, T. A. Graham, E. Élez, G. Argiles, P. Nuciforo, A. Sottoriva, R. Dienstmann, D. Pasini, E. Grassi, C. Isella, A. Bertotti, L. Trusolino, Colorectal cancer residual disease at maximal response to EGFR blockade displays a druggable Paneth cell-like phenotype., *Sci. Transl. Med.* **12** (2020), doi:10.1126/scitranslmed.aax8313.

28. H. Koch, M. E. D. C. Busto, K. Kramer, G. Médard, B. Kuster, Chemical Proteomics Uncovers EPHA2 as a Mechanism of Acquired Resistance to Small Molecule EGFR Kinase Inhibition, *J. Proteome Res.* **14**, 2617–2625 (2015).

29. A. Strimpakos, G. Pentheroudakis, V. Kotoula, W. De Roock, G. Kouvatseas, P. Papakostas, T. Makatsoris, D. Papamichael, A. Andreadou, J. Sgouros, A. Zizi-Sermpetzoglou, A. Kominea, D. Televantou, E. Razis, E. Galani, D. Pectasides, S. Tejpar, K. Syrigos, G. Fountzilas, The Prognostic Role of Ephrin A2 and Endothelial Growth Factor Receptor Pathway Mediators in Patients With Advanced Colorectal Cancer Treated With Cetuximab, *Clin. Colorectal Cancer* **12**, 267-274.e2 (2013).

30. P. D. Dunne, S. Dasgupta, J. K. Blayney, D. G. McArt, K. L. Redmond, J.-A. Weir, C. A. Bradley, T. Sasazuki, S. Shirasawa, T. Wang, S. Srivastava, C. W. Ong, K. Arthur, M. Salto-Tellez, R. H. Wilson, P. G. Johnston, S. Van Schaeybroeck, EphA2 Expression Is a Key Driver of Migration and Invasion and a Poor Prognostic Marker in Colorectal Cancer, *Clin. Cancer Res.* **22**, 230–242 (2016).

31. S. Heinzlmeir, D. Kudlinzki, S. Sreeramulu, S. Klaeger, S. L. Gande, V. Linhard, M. Wilhelm, H. Qiao, D. Helm, B. Ruprecht, K. Saxena, G. Médard, H. Schwalbe, B. Kuster, Chemical Proteomics and Structural Biology Define EPHA2 Inhibition by Clinical Kinase Drugs, *ACS Chem. Biol.* **11**, 3400–3411 (2016).

32. S. Klaeger, S. Heinzlmeir, M. Wilhelm, H. Polzer, B. Vick, P.-A. Koenig, M. Reinecke, B. Ruprecht, S. Petzoldt, C. Meng, J. Zecha, K. Reiter, H. Qiao, D. Helm, H. Koch, M. Schoof, G. Canevari, E. Casale, S. R. Depaolini, A. Feuchtinger, Z. Wu, T. Schmidt, L. Rueckert, W. Becker, J. Huenges, A.-K. Garz, B.-O. Gohlke, D. P. Zolg, G. Kayser, T. Vooder, R. Preissner, H. Hahne, N. Tõnisson, K. Kramer, K. Götze, F. Bassermann, J. Schlegl, H.-C. Ehrlich, S. Aiche, A. Walch, P. A. Greif, S. Schneider, E. R. Felder, J. Ruland, G. Médard, I. Jeremias, K. Spiekermann, B. Kuster, The target landscape of clinical kinase drugs, *Science (80-.).* **358**, eaan4368 (2017).

33. M. I. Davis, J. P. Hunt, S. Herrgard, P. Ciceri, L. M. Wodicka, G. Pallares, M. Hocker, D. K.

Treiber, P. P. Zarrinkar, Comprehensive analysis of kinase inhibitor selectivity, *Nat. Biotechnol.* **29**, 1046–1051 (2011).

34. T. A. Martin, W. G. Jiang, Loss of tight junction barrier function and its role in cancer metastasis, *Biochim. Biophys. Acta - Biomembr.* **1788**, 872–891 (2009).

35. A. O. Leech, R. G. B. Cruz, A. D. K. Hill, A. M. Hopkins, Paradigms lost-an emerging role for over-expression of tight junction adhesion proteins in cancer pathogenesis., *Ann. Transl. Med.* **3**, 184 (2015).

36. R. Pike, E. Ortiz-Zapater, B. Lumicisi, G. Santis, M. Parsons, KIF22 coordinates CAR and EGFR dynamics to promote cancer cell proliferation, *Sci. Signal.* **11** (2018), doi:10.1126/scisignal.aaq1060.

37. M. Hüttemann, I. Lee, L. Samavati, H. Yu, J. W. Doan, Regulation of mitochondrial oxidative phosphorylation through cell signaling, *Biochim. Biophys. Acta - Mol. Cell Res.* **1773**, 1701–1720 (2007).

38. R. Solmi, M. Lauriola, M. Francesconi, D. Martini, M. Voltattorni, C. Ceccarelli, G. Ugolini, G. Rosati, S. Zanotti, I. Montroni, G. Mattei, M. Taffurelli, D. Santini, F. Pezzetti, A. Ruggeri, G. Castellani, L. Guidotti, D. Coppola, P. Strippoli, Displayed correlation between gene expression profiles and submicroscopic alterations in response to cetuximab, gefitinib and EGF in human colon cancer cell lines, *BMC Cancer* **8**, 227 (2008).

39. F. Rolfs, S. R. Piersma, M. P. Dias, J. Jonkers, C. R. Jimenez, Feasibility of Phosphoproteomics on Leftover Samples After RNA Extraction With Guanidinium Thiocyanate, *Mol. Cell. Proteomics* **20**, 100078 (2021).

40. H. E. Francies, A. Barthorpe, A. McLaren-Douglas, W. J. Barendt, M. J. Garnett, in *Methods in Molecular Biology*, (2019), vol. 1576, pp. 339–351.

41. F. Galimi, D. Torti, F. Sassi, C. Isella, D. Cora, S. Gastaldi, D. Ribero, A. Muratore, P. Massucco, D. Siatis, G. Paraluppi, F. Gonella, F. Maione, A. Pisacane, E. David, B. Torchio, M. Risio, M. Salizzoni, L. Capussotti, T. Perera, E. Medico, M. F. Di Renzo, P. M. Comoglio, L. Trusolino, A. Bertotti, Genetic and Expression Analysis of MET, MACC1, and HGF in Metastatic Colorectal Cancer: Response to Met Inhibition in Patient Xenografts and Pathologic Correlations, *Clin. Cancer Res.* **17**, 3146–3156 (2011).

42. J. C. van der Mijn, M. Labots, S. R. Piersma, T. V. Pham, J. C. Knol, H. J. Broxterman, H. M. Verheul, C. R. Jiménez, Evaluation of different phospho-tyrosine antibodies for label-free phosphoproteomics, *J. Proteomics* **127**, 259–263 (2015).

43. S. R. Piersma, J. C. Knol, I. de Reus, M. Labots, B. K. Sampadi, T. V Pham, Y. Ishihama, H. M. W. Verheul, C. R. Jimenez, Feasibility of label-free phosphoproteomics and application to base-line signaling of colorectal cancer cell lines, *J. Proteomics* **127**, 247–258 (2015).

44. N. Sugiyama, T. Masuda, K. Shinoda, A. Nakamura, M. Tomita, Y. Ishihama, Phosphopeptide Enrichment by Aliphatic Hydroxy Acid-modified Metal Oxide Chromatography for Nano-LC-MS/MS in Proteomics Applications, *Mol. Cell. Proteomics* **6**, 1103–1109 (2007).

45. P. V. Hornbeck, B. Zhang, B. Murray, J. M. Kornhauser, V. Latham, E. Skrzypek, PhosphoSitePlus, 2014: Mutations, PTMs and recalibrations, *Nucleic Acids Res.* **43**, D512–D520 (2015).

46. G. Manning, D. B. Whyte, R. Martinez, T. Hunter, S. Sudarsanam, The protein kinase complement of the human genome., *Science* **298**, 1912–34 (2002).

47. B. Yates, B. Braschi, K. A. Gray, R. L. Seal, S. Tweedie, E. A. Bruford, Genenames.org: the HGNC and VGNC resources in 2017, *Nucleic Acids Res.* **45**, D619–D625 (2017).

48. M. E. Ritchie, B. Phipson, D. Wu, Y. Hu, C. W. Law, W. Shi, G. K. Smyth, limma powers differential expression analyses for RNA-sequencing and microarray studies, *Nucleic Acids Res.* **43**, e47–e47 (2015).

49. T. V Pham, C. R. Jimenez, An accurate paired sample test for count data, *Bioinformatics* **28**, i596–i602 (2012).

50. Z. Gu, R. Eils, M. Schlesner, Complex heatmaps reveal patterns and correlations in multidimensional genomic data, *Bioinformatics* **32**, 2847–2849 (2016).

51. Y. Benjamini, Y. Hochberg, Controlling the False Discovery Rate: A Practical and Powerful Approach to Multiple Testing, *J. R. Stat. Soc. Ser. B* **57**, 289–300 (1995).

52. G. Korotkevich, V. Sukhov, N. Budin, B. Shpak, M. Artyomov, A. Sergushichev, Fast gene set enrichment analysis, (2016), doi:10.1101/060012.

53. R. A. M. Villanueva, Z. J. Chen, ggplot2: Elegant Graphics for Data Analysis (2nd ed.), *Meas. Interdiscip. Res. Perspect.* **17**, 160–167 (2019).

54. K. Krug, P. Mertins, B. Zhang, P. Hornbeck, R. Raju, R. Ahmad, M. Szucs, F. Mundt, D. Forestier, J. Jane-Valbuena, H. Keshishian, M. A. Gillette, P. Tamayo, J. P. Mesirov, J. D. Jaffe, S. Carr, D. R. Mani, A Curated Resource for Phosphosite-specific Signature Analysis, *Mol. Cell. Proteomics* **18**, 576–593 (2019).

55. OLIVEROS, J. C., J. C. Oliveros, VENNY. An interactive tool for comparing lists with Venn diagrams, *http://bioinfogp.cnb.csic.es/tools/venny/index.html* (2016) (available at http://bioinfogp.cnb.csic.es/tools/venny/index.html (2007)).

56. D. Szklarczyk, A. L. Gable, K. C. Nastou, D. Lyon, R. Kirsch, S. Pyysalo, N. T. Doncheva, M. Legeay, T. Fang, P. Bork, L. J. Jensen, C. von Mering, The STRING database in 2021: Customizable protein-protein networks, and functional characterization of user-uploaded gene/measurement sets, *Nucleic Acids Res.* **49**, D605–D612 (2021).

57. P. Shannon, A. Markiel, O. Ozier, N. S. Baliga, J. T. Wang, D. Ramage, N. Amin, B. Schwikowski, T. Ideker, Cytoscape: a software environment for integrated models of biomolecular interaction networks., *Genome Res.* **13**, 2498–504 (2003).

58. M. Legeay, N. T. Doncheva, J. H. Morris, L. J. Jensen, Visualize omics data on networks with Omics Visualizer, a Cytoscape App, *F1000Research* **9**, 1–17 (2020).

59. J. H. Morris, L. Apeltsin, A. M. Newman, J. Baumbach, T. Wittkop, G. Su, G. D. Bader, T. E. Ferrin, ClusterMaker: A multi-algorithm clustering plugin for Cytoscape, *BMC Bioinformatics* **12**, 1–14 (2011).

60. S. Maere, K. Heymans, M. Kuiper, BiNGO: A Cytoscape plugin to assess overrepresentation of Gene Ontology categories in Biological Networks, *Bioinformatics* **21**, 3448–3449 (2005).

61. Y. Perez-Riverol, A. Csordas, J. Bai, M. Bernal-Llinares, S. Hewapathirana, D. J. Kundu, A. Inuganti, J. Griss, G. Mayer, M. Eisenacher, E. Pérez, J. Uszkoreit, J. Pfeuffer, T. Sachsenberg,

Ş. Yılmaz, S. Tiwary, J. Cox, E. Audain, M. Walzer, A. F. Jarnuczak, T. Ternent, A. Brazma, J. A. Vizcaíno, The PRIDE database and related tools and resources in 2019: improving support for quantification data, *Nucleic Acids Res.* **47**, D442–D450 (2019).

62. J. M. Carboni, M. Wittman, Z. Yang, F. Lee, A. Greer, W. Hurlburt, S. Hillerman, C. Cao, G. H. Cantor, J. Dell-John, C. Chen, L. Discenza, K. Menard, A. Li, G. Trainor, D. Vyas, R. Kramer, R. M. Attar, M. M. Gottardis, BMS-754807, a small molecule inhibitor of insulin-like growth factor-1R/IR., *Mol. Cancer Ther.* **8**, 3341–9 (2009).

63. M. J. Mulvihill, A. Cooke, M. Rosenfeld-Franklin, E. Buck, K. Foreman, D. Landfair, M. O'Connor, C. Pirritt, Y. Sun, Y. Yao, L. D. Arnold, N. W. Gibson, Q.-S. Ji, Discovery of OSI-906: a selective and orally efficacious dual inhibitor of the IGF-1 receptor and insulin receptor., *Future Med. Chem.* **1**, 1153–71 (2009).

Acknowledgments:

VitrOmics Healthcare Services (VHS), Cancer Center Amsterdam and Netherlands Organisation for Scientific Research (NWO- Middelgroot project number 91116017) are acknowledged for support of the mass spectrometry infrastructure and Surfsara for computing infrastructure (reference e-infra180166). Furthermore, we thank both Cancer Center Amsterdam and René Vogels Stichting for providing a travel grant for RB and Dutch Cancer Society grant KWF 12516 for support of FB.

Funding:

Dutch Cancer Society grant KWF 12516 (to C.R.J.); AIRC, Associazione Italiana per la Ricerca sul Cancro, Investigator Grants 20697 (to A.B.) and 22802 (to L.T.); AIRC 5x1000 grant 21091 (to A.B. and L.T.); AIRC/CRUK/FC AECC Accelerator Award 22795 (to L.T.); European Research Council Consolidator Grant 724748 BEAT (to A.B.); H2020 grant agreement no. 754923 COLOSSUS (to L.T.); H2020 INFRAIA grant agreement no. 731105 EDIReX (to A.B.); and Fondazione Piemontese per la Ricerca sul Cancro-ONLUS, 5x1000 Ministero della Salute 2016 (to L.T.).

Author contributions:

L.T. and A.B. generated and provided patient-derived xenografts (PDX). R.B. and R.G.H. performed tissue lysis and phosphopeptide enrichment. S.R.P. conducted LC-MS/MS measurements. S.R.P, J.C.K., A.A.H., and T.V.P. analyzed and processed LC-MS/MS data for peptide identification and quantification. The (phospho)proteomics data was curated and annotated by R.B. and J.C.K. R.B. conducted 2-group comparisons, GSEA, and INKA analysis. F.B. performed PTM-SEA analysis. A.A.H. cross-checked the phosphoproteome results against combined human-mouse peptide identification and quantification. M.V. and E.G. analyzed RNAseq data. V.V., F.C., and B.L. generated organoids from PDX models. R.B. conducted organoid cell viability assays. E.R.Z. and G.M. performed and analyzed in vivo PDX experiments. C.R.J., H.M.W.V., L.T., A.B., and M.L. conceived and supervised the project. C.R.J., L.T., and A.B. acquired funding. R.B. wrote the manuscript. R.B., J.C.K., F.B., and A.A.H. created the figures. C.R.J., H.M.W.V., L.T., A.B., and M.L. reviewed and edited the manuscript. The final manuscript was approved by all co-authors.

Competing interests: Authors declare that they have no competing interests.

Data and materials availability:

All data associated with this study are in the paper or supplementary materials. The mass spectrometry proteomics data have been deposited to the ProteomeXchange Consortium trough the PRIDE *(61)* partner repository with the dataset identifier PXD029127 for the main dataset and PXD029299 for the organoid dataset. RNAseq data have been deposited in the European Genome-Phenome Archive (EGA) under accession code EGAS00001006492. Access to these data will be granted upon registration to EGA and request to access these studies. Processed expression levels and raw read counts are publicly available in GEO (GSE204805). PDX models and derivatives thereof are available for solely academic purposes from L.T. or A.B. under a material transfer agreement with the University of Torino.

Figures

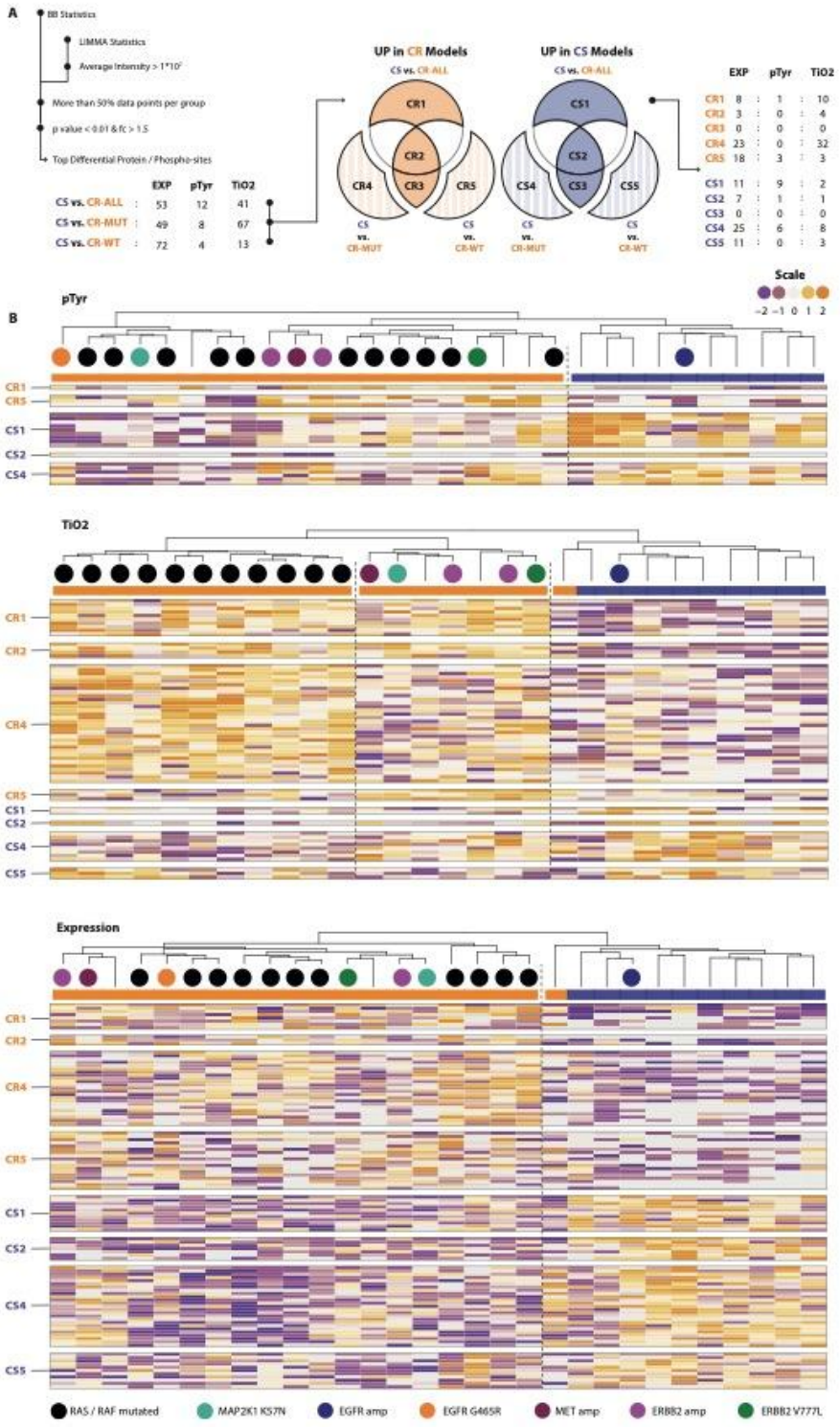
A
BB Statistics
LIMMA Statistics
Average Intensity > 1*10^7
More than 50% data points per group
p value < 0.01 & fc > 1.5
Top Differential Protein / Phospho-sites
EXP pTyr TiO2
CS vs. CR-ALL : 53 12 41
CS vs. CR-MUT : 49 8 67
CS vs. CR-WT : 72 4 13
UP in CR Models
CS vs. CR-ALL
CR1
CR2
CR3
CR4
CR5
CS vs. CR-MUT
CS vs. CR-WT
UP in CS Models
CS vs. CR-ALL
CS1
CS2
CS3
CS4
CS5
CS vs. CR-MUT
CS vs. CR-WT
EXP pTyr TiO2
CR1 8 : 1 : 10
CR2 3 : 0 : 4
CR3 0 : 0 : 0
CR4 23 : 0 : 32
CR5 18 : 3 : 3
CS1 11 : 9 : 2
CS2 7 : 1 : 1
CS3 0 : 0 : 0
CS4 25 : 6 : 8
CS5 11 : 0 : 3
B
pTyr
Scale
−2 −1 0 1 2
CR1
CR3
CS1
CS2
CS4
TiO2
CR1
CR2
CR4
CR5
CS1
CS2
CS4
CS5
Expression
CR1
CR2
CR4
CR5
CS1
CS2
CS4
CS5
RAS / RAF mutated
MAP2K1 K57N
EGFR amp
EGFR G465R
MET amp
ERBB2 amp
ERBB2 V777L

Fig. 1. Comparative analysis of sensitive and resistant PDX models to cetuximab identifies a differential signature. (A), Overview of group comparison of identified phospho-sites using LIMMA statistics between cetuximab sensitive models (CS) versus all resistant models (CR ALL), versus the resistant models wild-type for mutations in RAS/RAF (CR WT) or versus the RAS/RAF-mutated resistant models (CR MUT). LIMMA results where filtered for each comparison. Overlap between these comparisons shows differential phospho-sites that are more distinctive for the general comparison CR ALL versus sensitive (S/R1, S/R2, S/R3) whereas parts without overlap (S/R4 and S/R5) are distinctive for respectively CR WT and CR MUT. **(B)**, Clustering of the combined signature of the top differential phospho-sites (rows) from the comparisons in the pTyr (top), TiO2 (middle) and Expression (bottom) datasets. Response is indicated for sensitive (blue) and resistant (orange) models. Genomic aberrations of models are indicated with colored circles below. Clustering shows separation between sensitive and resistant models in pTyr and near-complete separation in TiO2 and Expression with separate clusters for RES WT and RES MUT in TiO2.

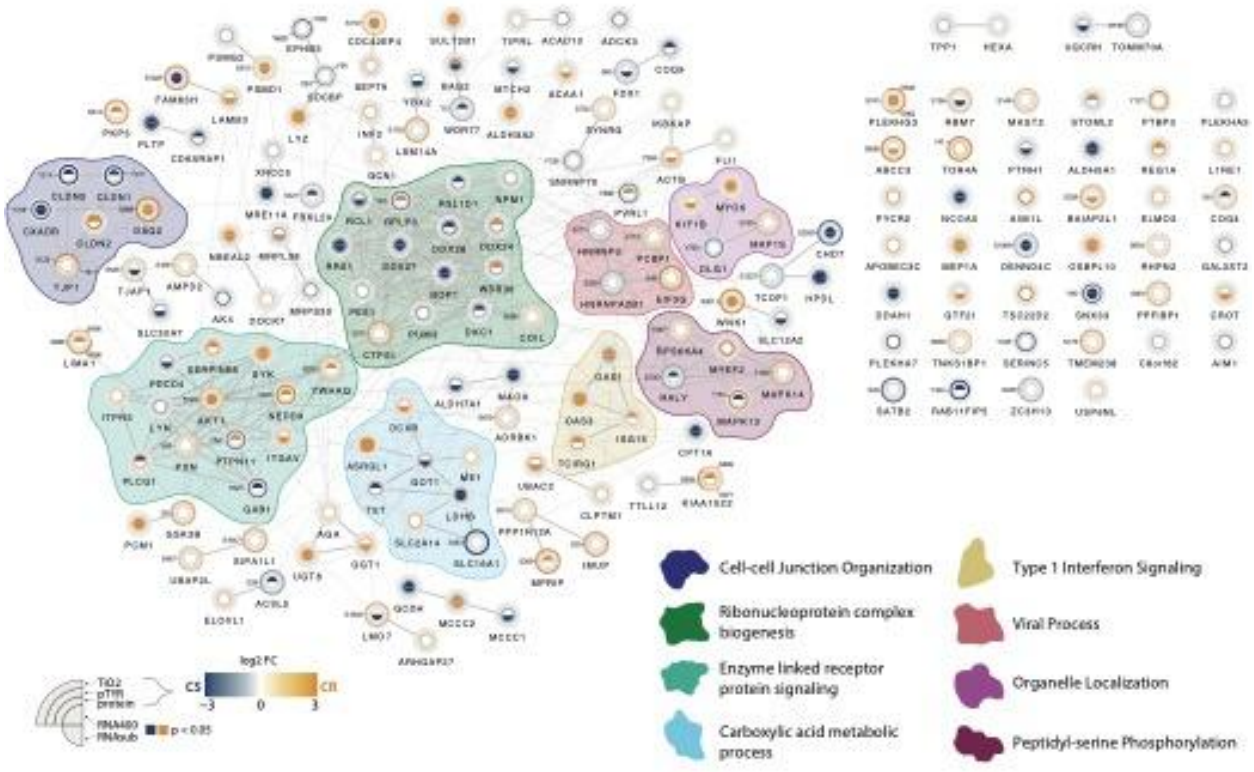

Fig. 2. Interaction network of proteins associated with cetuximab sensitivity and resistance. Previous group comparisons of cetuximab sensitive versus resistant tumors (CS vs. either CR ALL, CR MUT, and CR WT) were merged on CS versus CR. The maximum fold change among these three comparisons was log2-transformed and used to color-code a donut ring around the pertinent network node for every protein and a section of the ring for each phosphosite. Donut rings represent protein expression (inner ring), TiO2 (middle ring), and pTyr (outer ring). If any of the comparisons were significant ($p < 0.05$), the associated ring was colored a hue of orange (CR) or blue (CS), depending on the direction and fold change in the CS vs. CR-ALL comparisons. The inner circle represents significant genes (p-value < 0.05) from mRNA analysis comparing the models in this cohort (RNAsub, bottom halve of the inner circle) and a more extensive comparison between 157 cetuximab sensitive and 246 cetuximab resistant PDX tumors (RNA400, top halve of the inner circle). All (phospho)proteins were used to retrieve protein-protein associations from the STRING database v11, proteins without association are shown in the top right corner. Protein clusters were identified using the MCL algorithm of the clusterMaker2 app inside Cytoscape, and gene ontology analysis was performed with the BiNGO app using ontology definitions of April 2020 to analyze biology covered in this network.

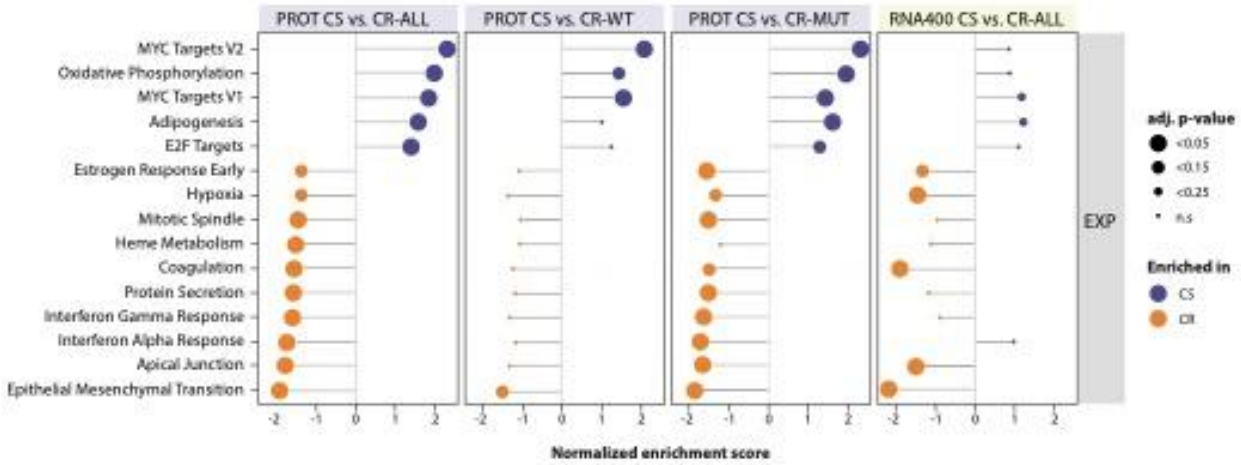

Fig. 3. Protein expression-driven enrichment of cetuximab sensitive and cetuximab resistant biology. Lollipop plots showing amount of enrichment as the normalized enrichment scores on the x-axis of differentially regulated protein expression-driven HALLMARK signatures between cetuximab sensitive (CS) and cetuximab resistant (CR) PDX models as determined by gene set enrichment analysis (GSEA). The analysis utilized genes ranked according log-transformed and signed p-values obtained from all protein expression (PROT) comparisons between CS and CR, as well as the RNA400 CS versus CR-all comparison. The C5 ontology gene sets collection from the MSigDB v7.2 database served as input files. The size of the circles corresponds to significance of enrichment with blue indicating enrichment in CS and orange indicating enrichment in CR tumors. Shown are processes that have at least a adj. p-value less than 0.15 in protein expression (PROT) CS vs. CR-ALL comparison.

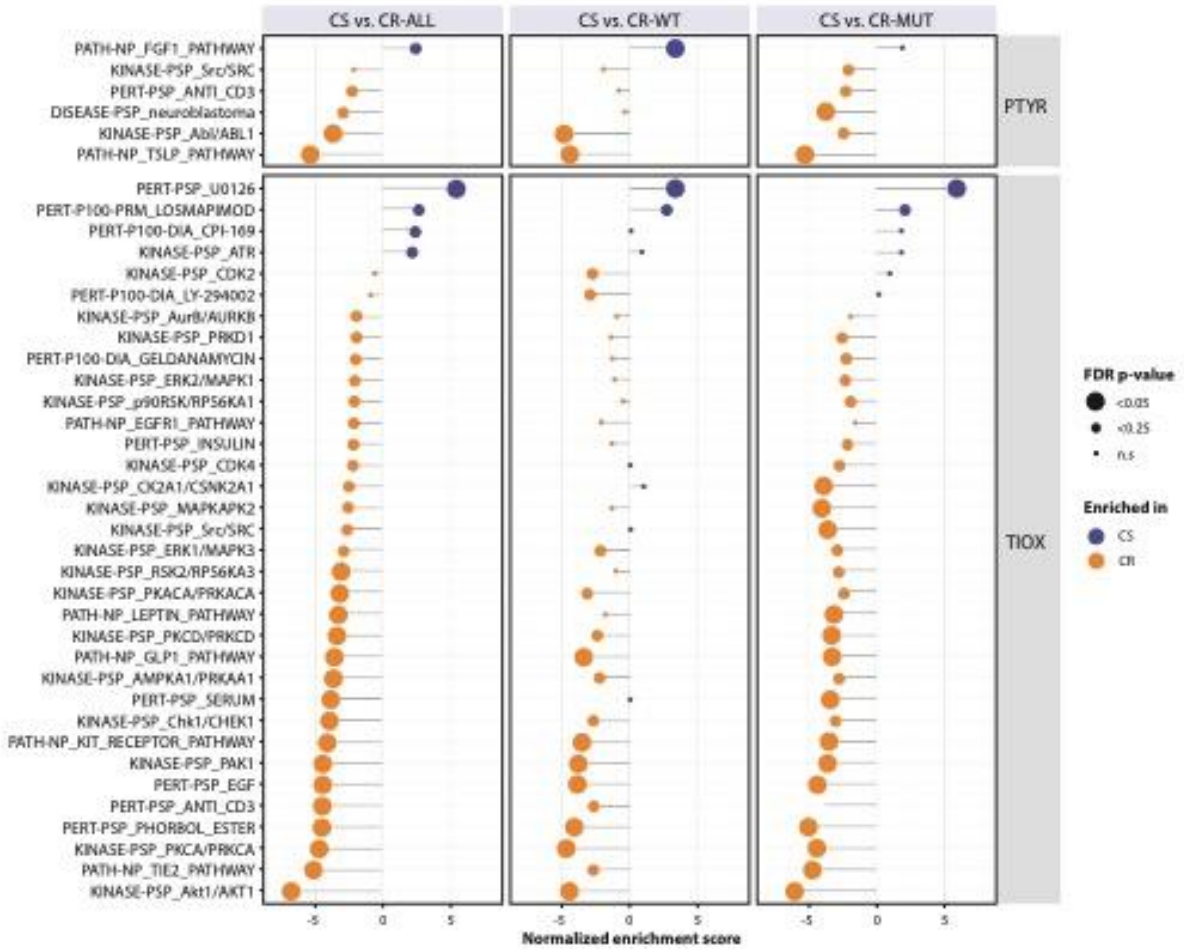

Fig. 4. Post-translational modification signature enrichment analysis of cetuximab sensitive and cetuximab resistant biology. Lollipop plots showing amount of enrichment as the normalized enrichment scores on the x-axis of differentially regulated phosphosite-driven signatures between CS (blue) and CR (orange) PDX models as determined by post-translational modification signature enrichment analysis (PTM-SEA). The analysis utilized phosphosites ranked according log-transformed and signed p-values obtained from all pTyr and Tio2 comparisons. The size of the circles corresponds to significance of enrichment; shown are all signatures with FDR-adjusted *P*-value < 0.25.

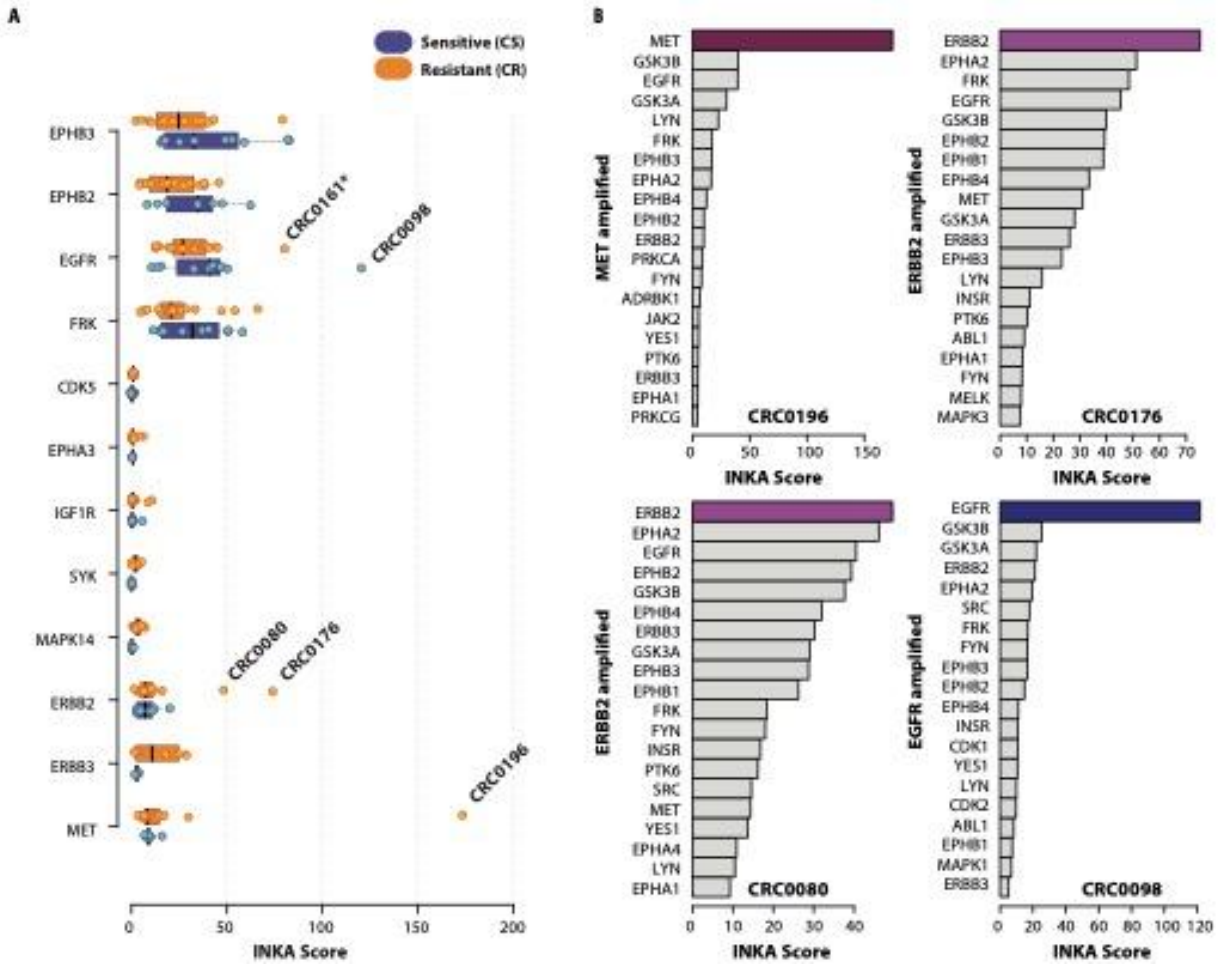

Fig. 5. INKA analysis of resistant models reveals hyper-active kinases. (A), Boxplot depicting mean INKA score of CS (blue) and CR models (orange), only kinases with more than 25% difference between CS and CR and measured in more than 5 models are shown. Dots indicate individual PDX models. (*) model CRC161 with unknown mechanism of cetuximab resistance. **(B)** INKA bar plots of models CRC0196 (top left), CRC0176 (top right), CRC0080 (bottom left) and CRC0098 (bottom right) with hyper active kinases. Overview of all INKA bar plots including plots in this figure are shown in fig. S10 & fig. S11.

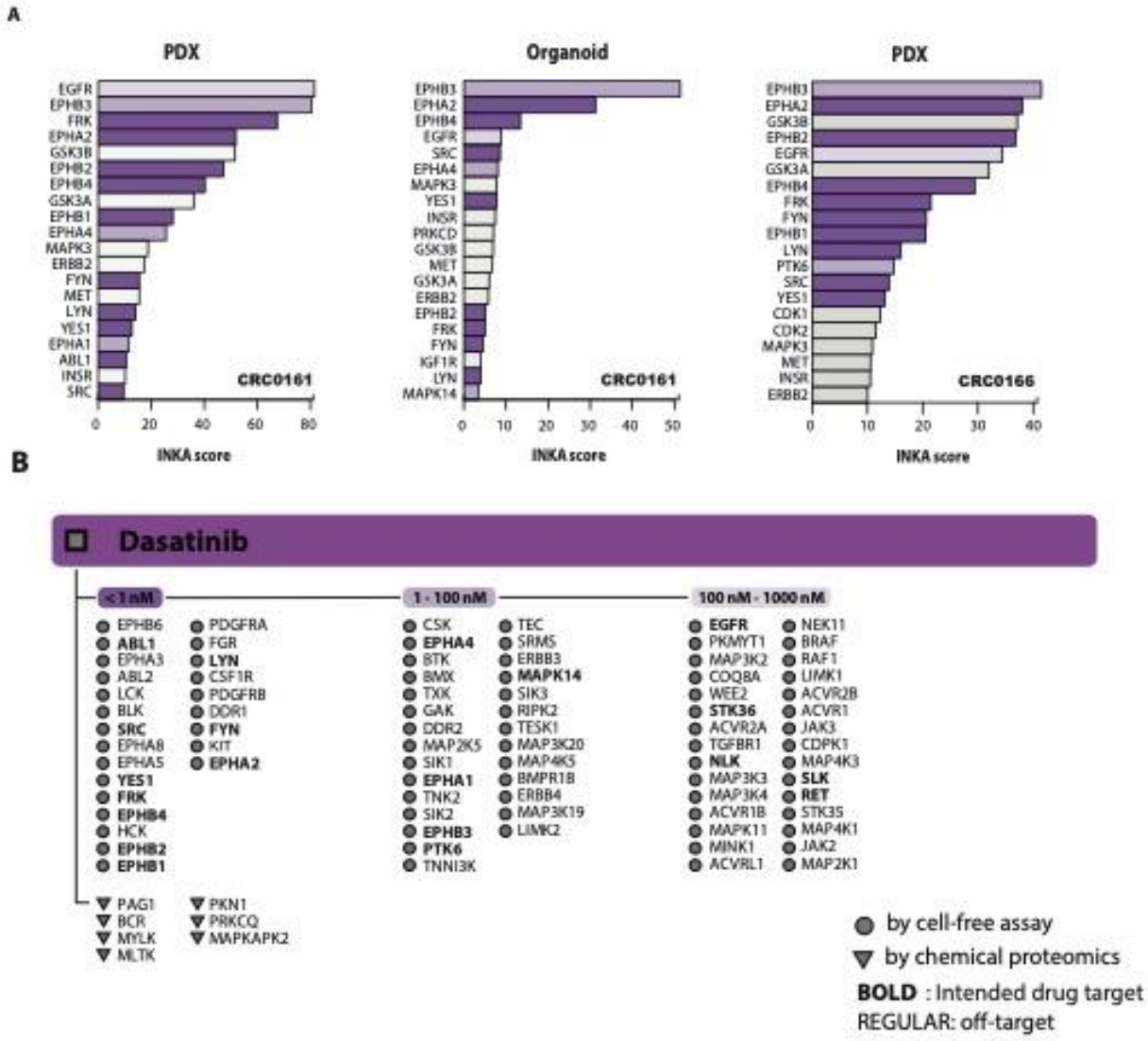

Fig. 6. INKA analysis of models with unknown mechanism of cetuximab resistance reveal dasatinib as a potential treatment. (A), INferred Kinase Activity (INKA) profiles of unexplained resistant PDX tumors CRC0161 (left) CRC0166 (right) and corresponding organoid culture of CRC0161 (middle). Targets of dasatinib are indicated in purple (dark purple: affinity < 1nM, medium: affinity 1 - 100nM, light: affinity 100 - 1000nM). All INKA bar plots including plots in this figure are shown in fig. S10 & fig. S11. **(B)** Overview of experimentally established targets of dasatinib with an affinity in the nanomolar range. Targets denoted by triangles were discovered using a chemical proteomics approach *(32)*, and those denoted by circles were identified using cell-free assays *(33, 62, 63)*.

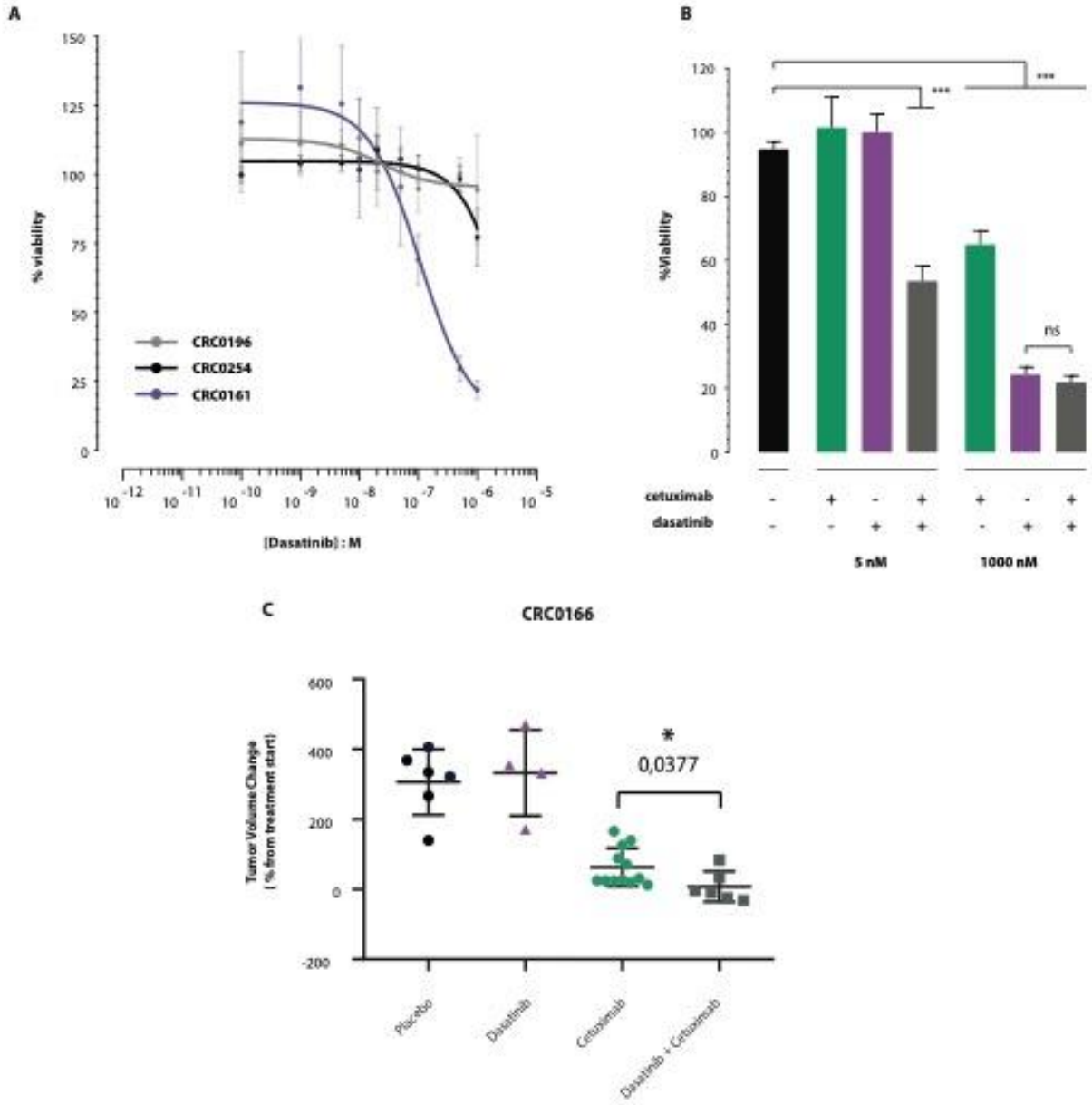

Fig. 7. Organoid and PDX viability in response to dasatinib inhibition. (A) Organoid viability in response to dasatinib inhibition was tested in three organoids: CRC0196 (low target expression, n = 6), CRC0254 (low target expression, n=6), and CRC0161 (high target expression, n = 6). Error bars represent SEM. **(B)** Viability of CRC0161 organoids at 5nM and 1000nM treated with Cetuximab (green, 5nM n = 2, 1000nM n = 6), Dasatinib (purple, 5nM n = 19, 1000nM n = 20), combination (grey, 5nM n = 4, 1000nM n = 6), no treatment (black, n= 18). Statistical analysis was performed using ordinary one-way ANOVA. Error bars represent SEM. Asterisks represent the level of significance (***p-value < 0.001). **(C)** Dot plot graph showing percentage tumor volume changes after three weeks of therapy with placebo, dasatinib (50 mg/kg by oral gavage, daily), cetuximab (20 mg/kg by intraperitoneal injection, twice-weekly) and the combination of dasatinib and cetuximab. NOD-SCID mice were inoculated subcutaneously with CRC0166 tumor fragments and randomized to the

different treatments when tumors reached an average volume of 400 mm^3. n = 4 to 12 animals per each treatment arm. Statistical analysis by two-tailed unpaired Welch's t-test.

Supplementary Figures

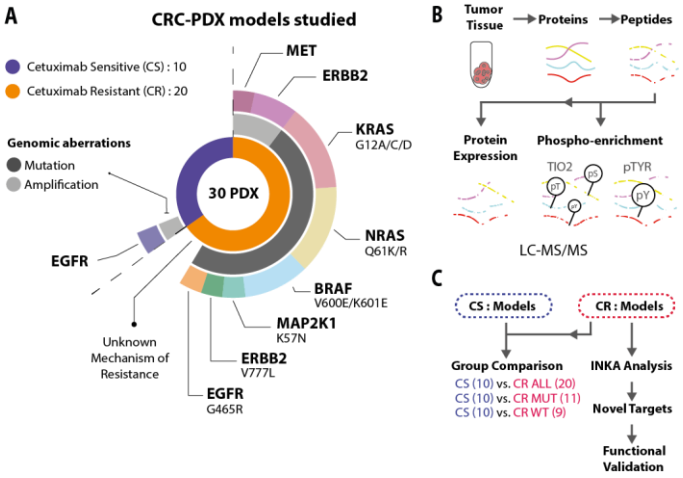

Suppl. Fig. 1. Phosphoproteomics identifies targets and markers associated with sensitivity and resistance to EGFR blockade in colorectal cancer. (A), Thirty mCRC-PDX models were profiled including 10 cetuximab-sensitive (green, inner ring) and 19 cetuximab-resistant xenograft tumors (red, inner ring). Resistance-associated genomic aberrations in resistant tumors included both mutations (black, middle ring) and amplifications (gray, middle ring). The outside ring shows known genomic aberrations associated with resistance to cetuximab **(B)**, LS-MS/MS phospho-proteomics and proteomics were used to profile both the proteome and phosphoproteome. This enabled the collection of three data sets: protein expression, global phosphoproteomics (TiO2), and phosphotyrosine-enriched phosphoproteomics (pTyr) **(C)**, Proteome and phosphoproteome data were used to make group-comparisons between cetuximab sensitive and resistant tumors to identify biomarkers of response. INKA analysis was done on individual tumors to find potential targets in cetuximab resistant tumors, followed by functional validation in PDX-derived organoids.

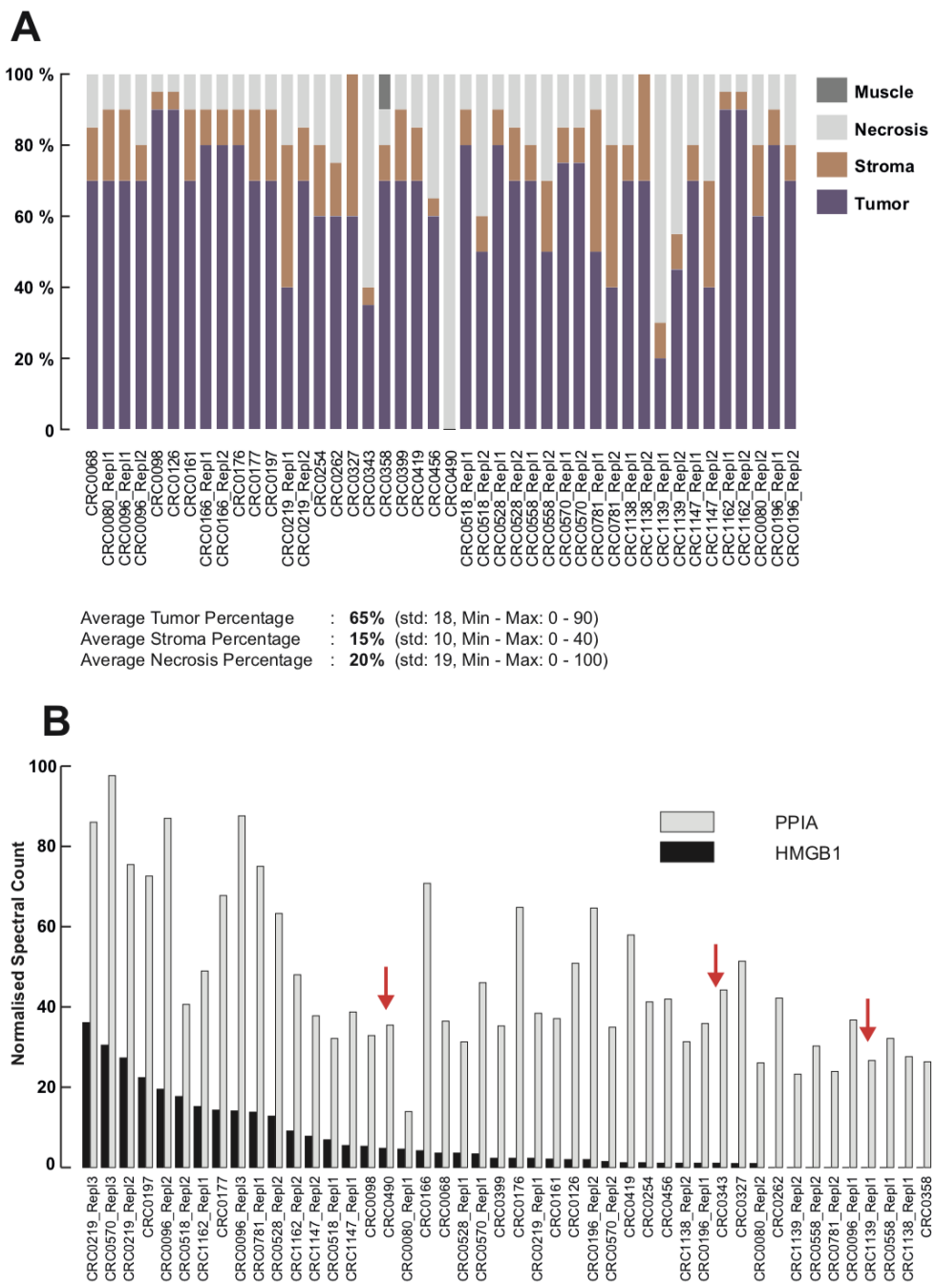

Suppl. Fig 2. Histological assessment of PDX tissue. (A), Overview of pathology report on HE stained representable sections of PDX tissue used for further (phospho) proteomics shows an average percentage of 65% epithelial cancer cells, 15% stroma and 20% necrosis. **(B),** Bar graph indicating expression data from proteomics analysis of two known protein markers for necrosis (PPIA, HMGB1). Red arrows indicate samples that based on pathology report showed high percentage of necrosis. Proteomic results show only average expression of necrosis markers in these models.

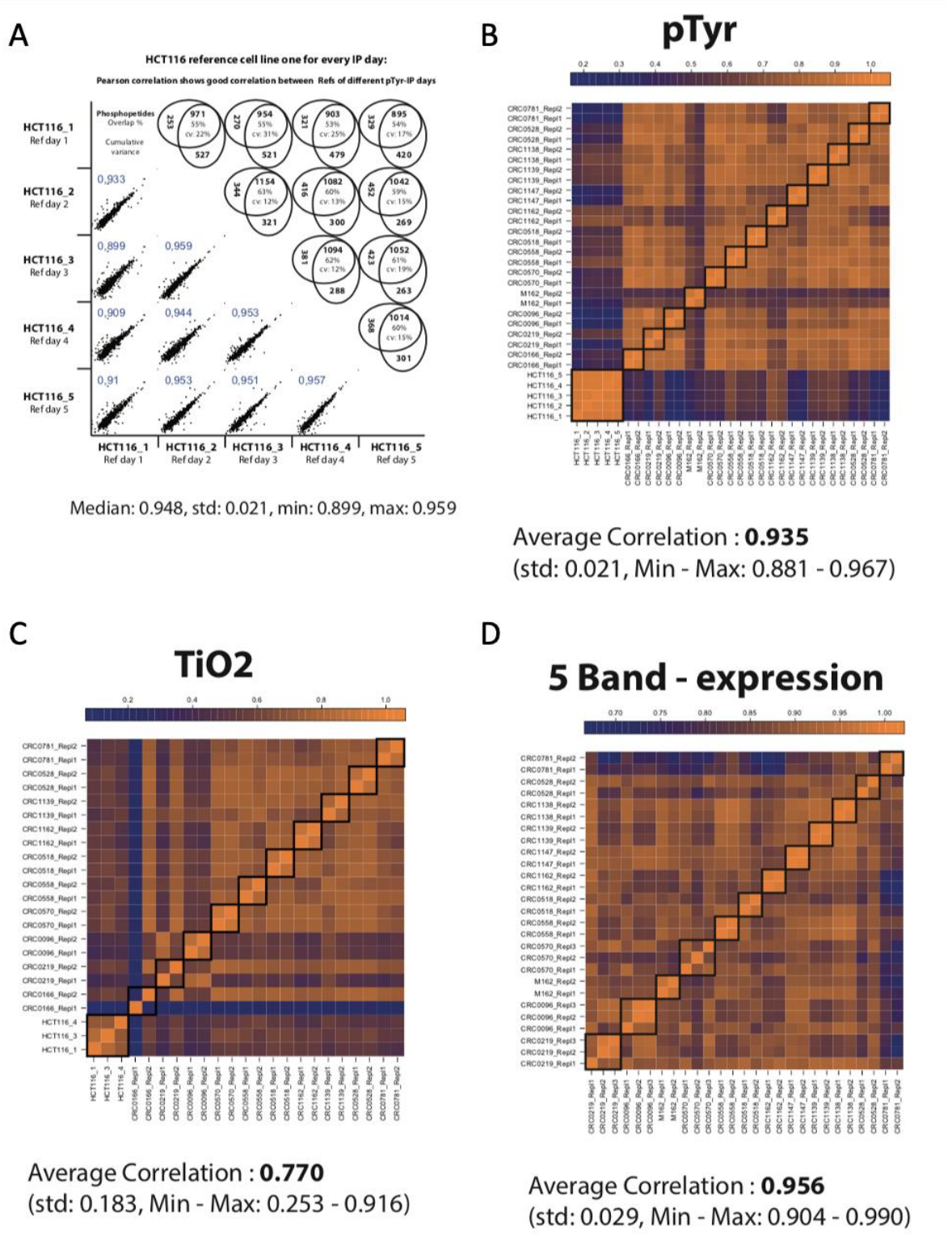

Suppl. Fig 3. Data reproducibility. (A), Pearson correlation and cumulative variance show high reproducibility between technical replicates. (**B**, **C** and **D**) biological replicates of PDX tumors (pTyr: 13 replicates, TIO2: 10 replicates, Expression: 12 replicates) clustered together in correlation clustering.

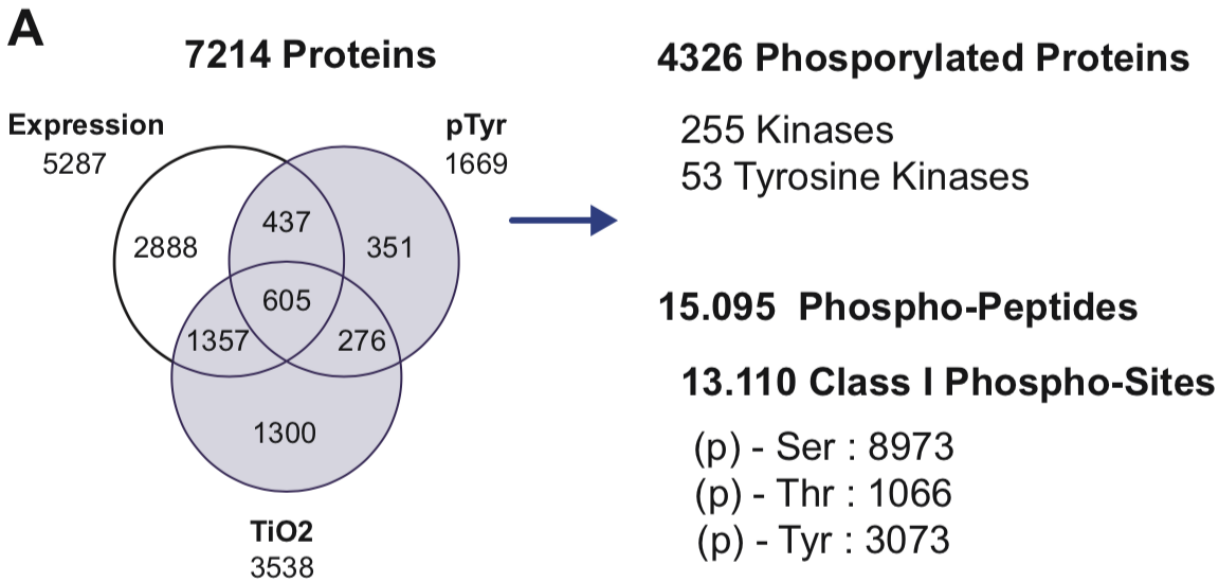

Suppl. Fig. 4. Overview (phospho) proteomics results. (A), The number of identified proteins and phosphoproteins in the total dataset using mass spectrometry-based expression proteomics, global and tyrosine phosphoproteomics.

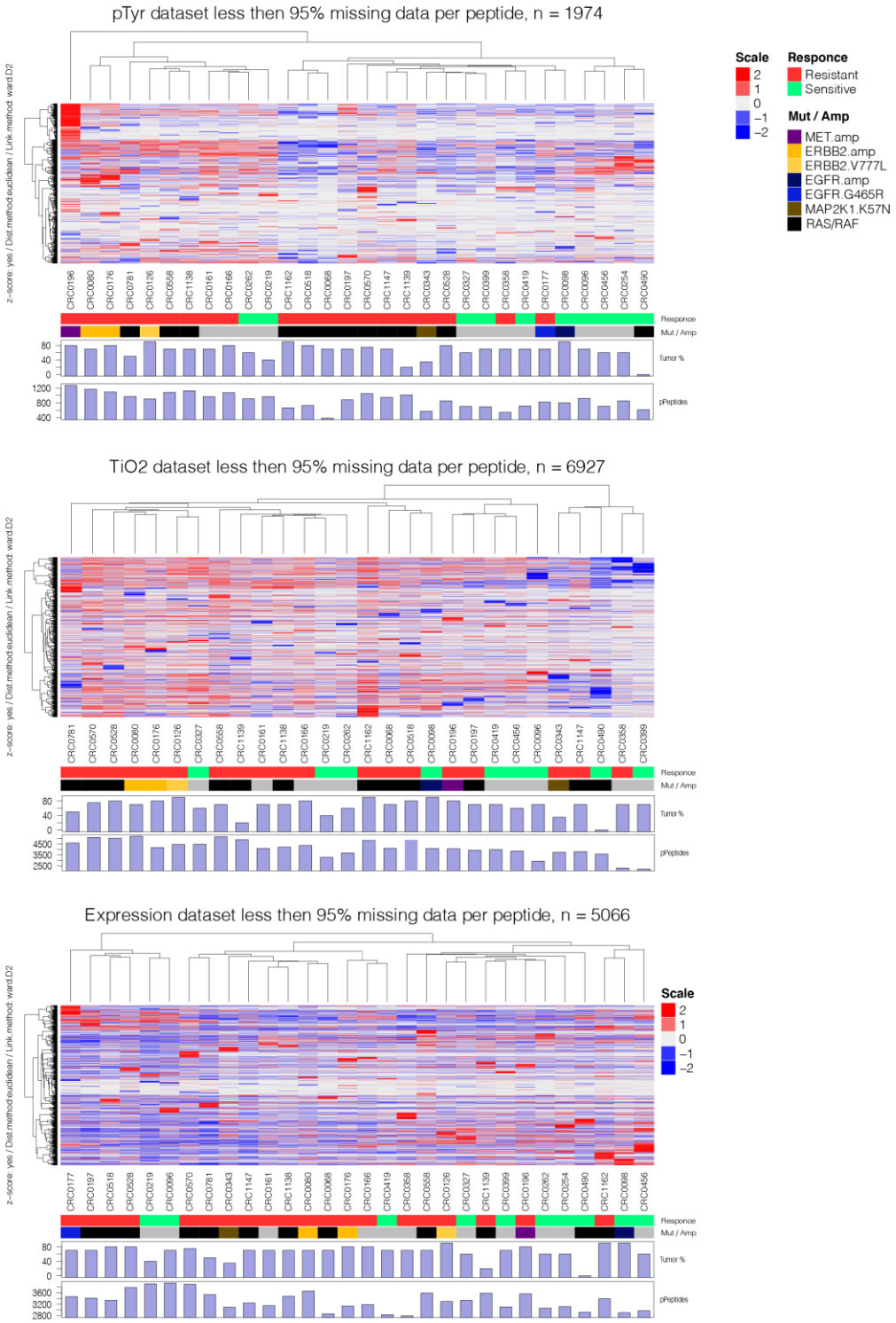

Suppl. Fig 5. Unsupervised clustering of datasets. Unsupervised clustering of tyrosine (pTyr) and global (TiO2) phosphoproteomics and protein expression dataset. Cluster were annotated with cetuximab response, genomic aberrations, tumor percentage and number of peptides. Clusters do not show sub-clustering of CS and CR tumors.

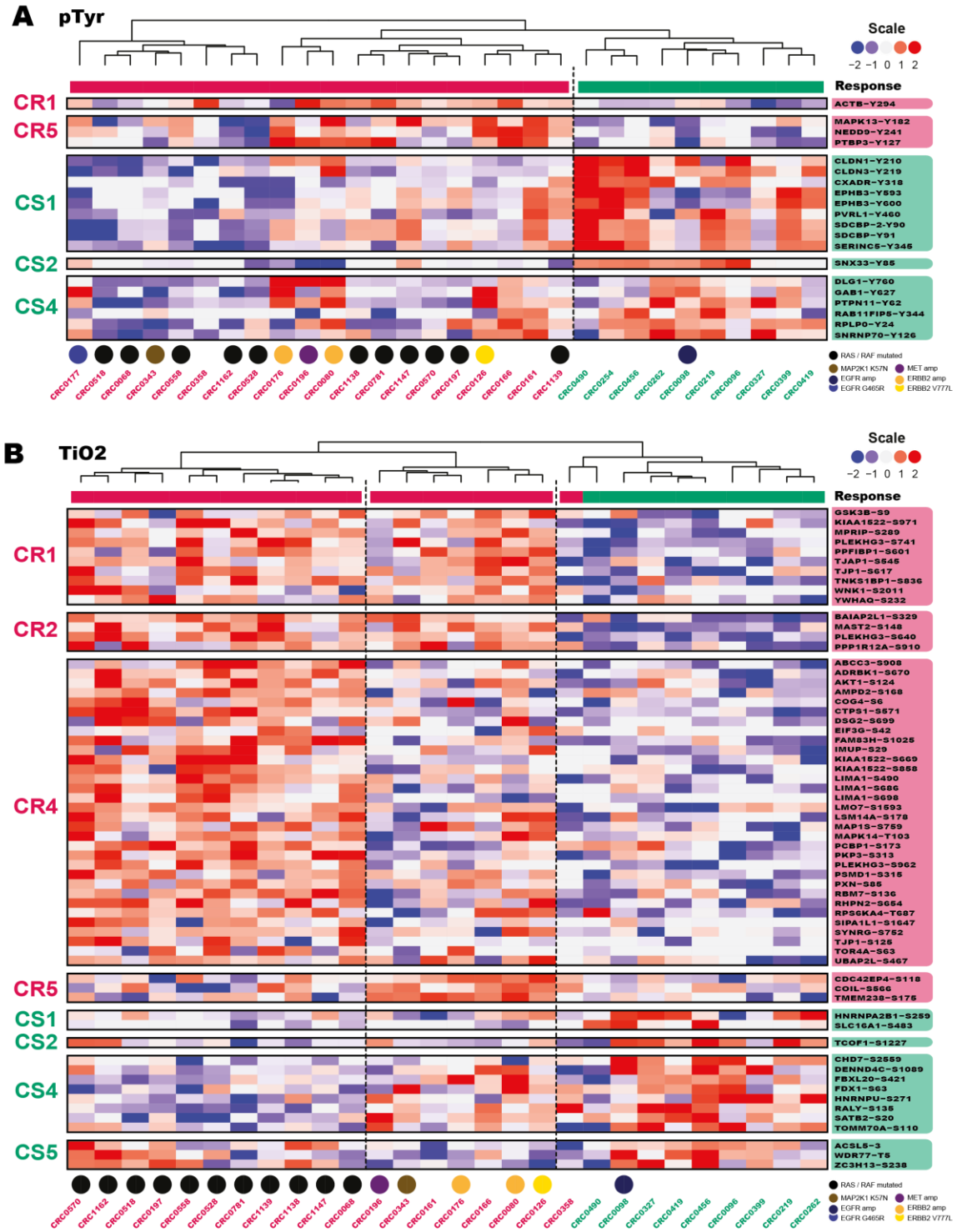
A
pTyr
Scale
−2 −1 0 1 2
Response
CR1
CR5
CS1
CS2
CS4
ACTB−Y294
MAPK13−Y182
NEDD9−Y241
PTBP3−Y127
CLDN1−Y210
CLDN3−Y219
CXADR−Y318
EPHB3−Y593
EPHB3−Y600
PVRL1−Y460
SDCBP−2−Y90
SDCBP−Y91
SERINC5−Y345
SNX33−Y85
DLG1−Y760
GAB1−Y627
PTPN11−Y62
RAB11FIP5−Y344
RPLP0−Y24
SNRNP70−Y126
RAS / RAF mutated
MAP2K1 K57N
MET amp
EGFR amp
ERBB2 amp
EGFR G465R
ERBB2 V777L
CRC0177
CRC0518
CRC0068
CRC0343
CRC0558
CRC0358
CRC1162
CRC0528
CRC0176
CRC0196
CRC0080
CRC1138
CRC0781
CRC1147
CRC0570
CRC0197
CRC0126
CRC0166
CRC0161
CRC1139
CRC0490
CRC0254
CRC0456
CRC0262
CRC0098
CRC0219
CRC0096
CRC0327
CRC0399
CRC0419
B
TiO2
Scale
−2 −1 0 1 2
Response
CR1
CR2
CR4
CR5
CS1
CS2
CS4
CS5
GSK3B−S9
KIAA1522−S971
MPRIP−S289
PLEKHG3−S741
PPFIBP1−S601
TJAP1−S545
TJP1−S617
TNKS1BP1−S836
WNK1−S2011
YWHAQ−S232
BAIAP2L1−S329
MAST2−S148
PLEKHG3−S640
PPP1R12A−S910
ABCC3−S908
ADRBK1−S670
AKT1−S124
AMPD2−S168
COG4−S6
CTPS1−S871
DSG2−S699
EIF3G−S42
FAM83H−S1025
IMUP−S29
KIAA1522−S669
KIAA1522−S858
LIMA1−S490
LIMA1−S686
LIMA1−S698
LMO7−S1593
LSM14A−S178
MAP1S−S759
MAPK14−T103
PCBP1−S173
PKP3−S313
PLEKHG3−S962
PSMD1−S316
PXN−S85
RBM7−S136
RHPN2−S654
RPS6KA4−T687
SIPA1L1−S1647
SYNRG−S752
TJP1−S126
TOR4A−S63
UBAP2L−S467
CDC42EP4−S118
COIL−S66
TMEM238−S175
HNRNPA2B1−S259
SLC16A1−S483
TCOF1−S1227
CHD7−S2559
DENND4C−S1089
FBXL20−S421
FDX1−S63
HNRNPU−S271
RALY−S136
SAT2−S20
TOMM70A−S110
ACSL5−3
WDR77−T5
ZC3H13−S238
RAS / RAF mutated
MAP2K1 K57N
MET amp
EGFR amp
ERBB2 amp
EGFR G465R
ERBB2 V777L
CRC0570
CRC1162
CRC0518
CRC0197
CRC0558
CRC0528
CRC0781
CRC1139
CRC1138
CRC1147
CRC0068
CRC0196
CRC0343
CRC0161
CRC0176
CRC0166
CRC0080
CRC0126
CRC0358
CRC0490
CRC0098
CRC0327
CRC0419
CRC0456
CRC0096
CRC0399
CRC0219
CRC0262

Suppl. Fig 6.

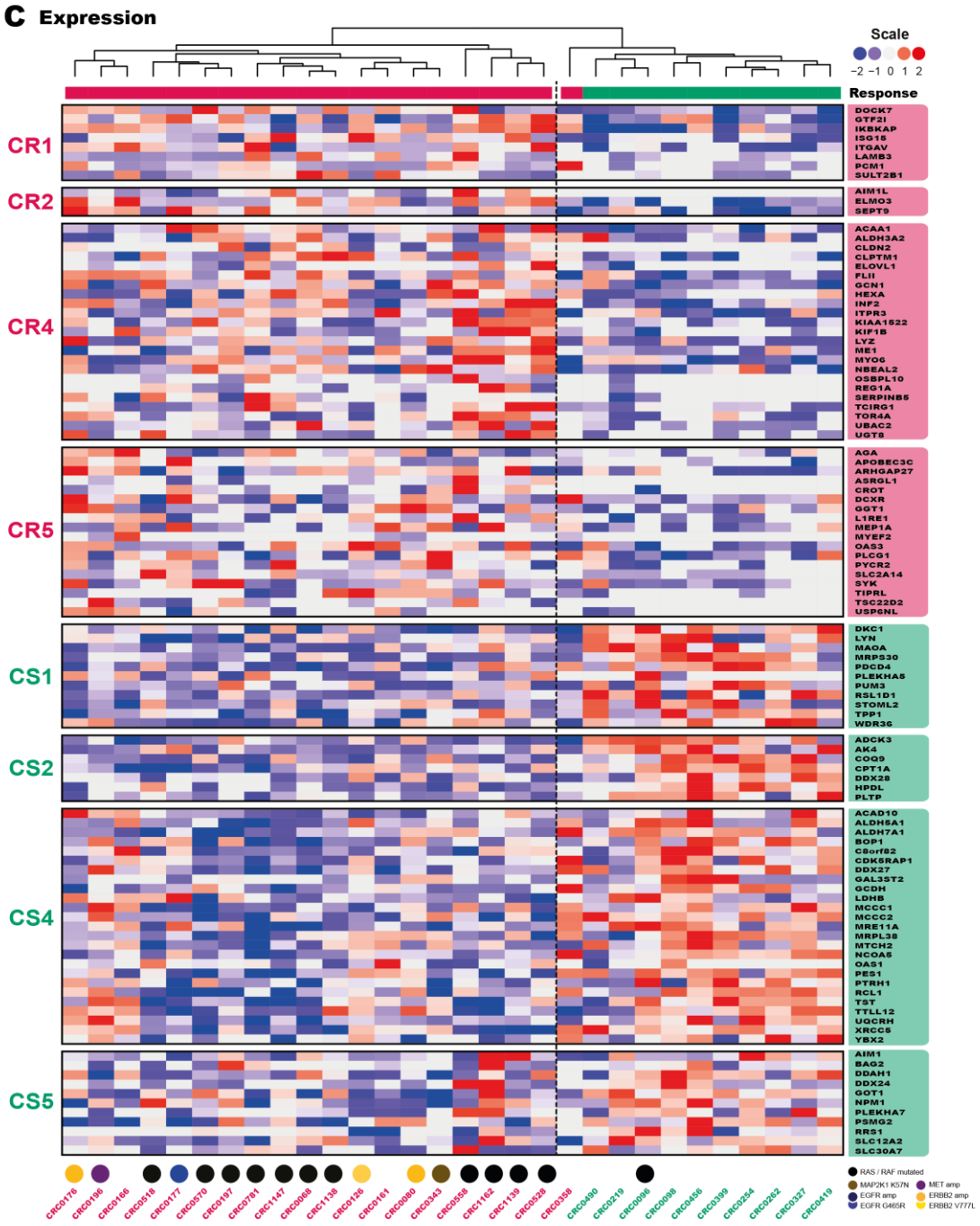

Suppl. Fig 6. Comparative analysis of PDX models sensitive and resistant to cetuximab identifies differential signature. Clustering of the combined signature of the top differential phospho-sites (rows) from the comparisons in the pTyr (**A**), TiO2 (**B**) and Expression (**C**) dataset. Response is indicated for sensitive (green) and resistant (red) models. Genomic aberrations of models are indicated with colored circles below. Clustering shows separation between sensitive and resistant models in pTyr and near-complete separation in TiO2 and Expression with separate clusters for RES WT and RES MUT in TiO2.

A

Overview number of models considered per comparison for protein and RNA expression data

	Comparison	Protein	RNA
1.	CS vs. CR-ALL	10 vs. 20	10 vs. 10
2.	CS vs. CR-WT	9 vs. 9	9 vs. 8
3.	CS vs. CR-MUT	9 vs. 11	(9 vs. 2)

No RNA-sequencing data was available for **9 CR-MUT** models. In addition, model CRC0358 (**CR-WT**) was not considered for RNA analyses due to outlier behavior. Due to the unbalanced and underpowered CS vs. CR-MUT comparison on RNA level, this comparison was excluded from all further analyses.

B

Overview number of models considered per comparison for protein phosphorylation data

	Comparison	pTyr	TiOx
1.	CS vs. CR-ALL	10 vs. 20	9 vs. 19
2.	CS vs. CR-WT	9 vs. 9	8 vs. 8
3.	CS vs. CR-MUT	9 vs. 11	9 vs. 11

No TiOx data was available for models CRC0254 (**CS-WT**) and CRC0177 (**CR-WT**) due to sample loss during TiOx enrichment

C

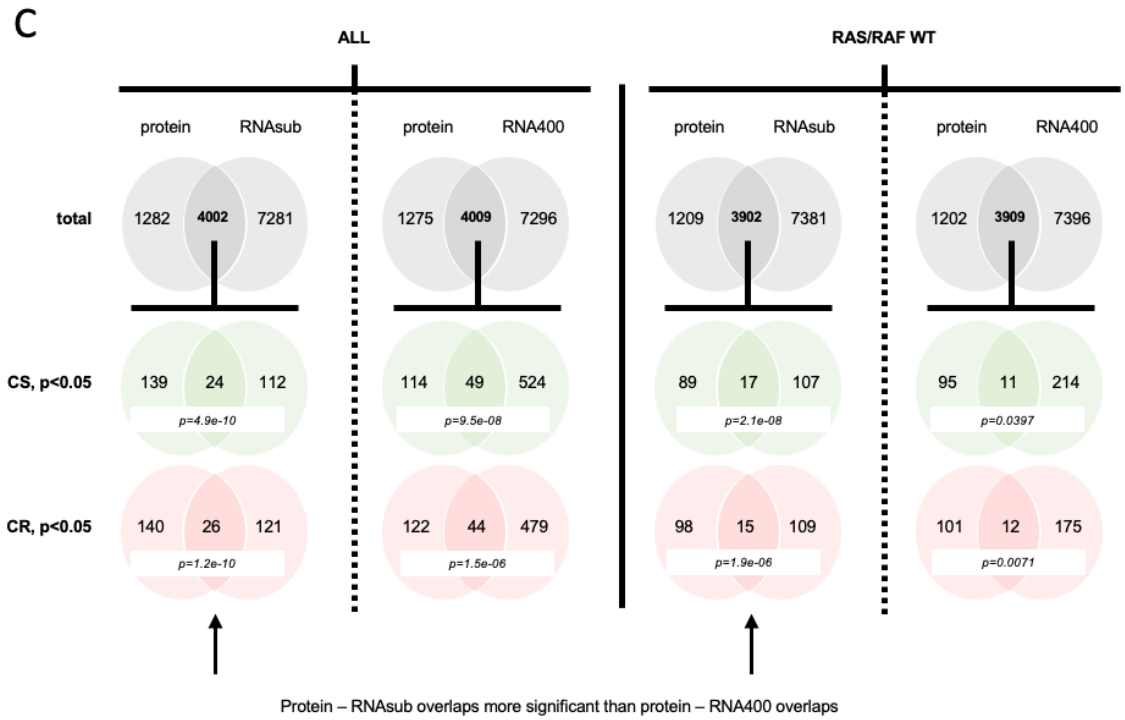

Suppl. Fig. 7. Overlap protein and RNAsub / RNA400 expression data. (A), Overview number of models considered per comparison for protein and RNA expression data. **(B),** Overview number of models considered per comparison for protein phosphorylation data**. (C),** Overlap in total identifications on protein and RNA level, and in significantly ($p<0.05$) differentially expressed genes between CS and CR PDX models. RNAsub refers to a comparison among the same subset of PDX models also used for proteomics profiling, RNA400 refers to a comparison among a large collection of ~400 PDX models (Isella et al., 2017). Hypergeometric test was performed to test for significance of overlap.

Type 1 Interferon Signaling

GO-ID	Description	p-val	corr p-val	cluster freq
45071	negative regulation of viral genome replication	1.5880E-7	2.4969E-5	3/4 75.0%
71357	cellular response to type I interferon	2.0110E-7	2.4969E-5	3/4 75.0%
50337	type I interferon signaling pathway	2.0110E-7	2.4969E-5	3/4 75.0%
34340	response to type I interferon	2.5031E-7	2.4969E-5	3/4 75.0%
1903901	negative regulation of viral life cycle	4.1431E-7	3.3062E-5	3/4 75.0%

Cell-cell Junction Organization

GO-ID	Description	p-val	corr p-val	cluster freq	total freq
45216	cell-cell junction organization	3.7658E-10	1.5892E-7	5/6 83.3%	165/17866 0..
98742	cell-cell adhesion via plasma-membrane adhesion molecules	3.4457E-9	7.2704E-7	5/6 83.3%	256/17866 1..
16338	calcium-independent cell-cell adhesion via plasma membrane cell-adhesion molecules	2.7928E-8	3.9224E-6	3/6 50.0%	21/17866 0....
2000810	regulation of bicellular tight junction assembly	3.7179E-8	3.9224E-6	3/6 50.0%	23/17866 0....

Ribonucleoprotein complex biogenesis

GO-ID	Description	p-val	corr p-val	cluster freq	total freq
22613	ribonucleoprotein complex biogenesis	1.2718E-17	7.0332E-15	12/15 80.0%	427/17866 2...
42254	ribosome biogenesis	2.9761E-17	8.2290E-15	11/15 73.3%	298/17866 1...
42273	ribosomal large subunit biogenesis	1.3075E-13	2.4102E-11	7/15 46.6%	77/17866 0....
6364	rRNA processing	2.2259E-12	3.0772E-10	8/15 53.3%	214/17866 1...
16072	rRNA metabolic process	3.4539E-12	3.8200E-10	8/15 53.3%	226/17866 1...

Enzyme linked receptor protein signaling

GO-ID	Description	p-val	corr p-val	cluster freq	total freq
7167	enzyme linked receptor protein signaling pathway	2.6502E-12	4.4311E-9	10/13 76.9%	718/17866 4.0%
7169	transmembrane receptor protein tyrosine kinase signaling pathway	8.5684E-12	7.1632E-9	9/13 69.2%	517/17866 2.8%
16477	cell migration	1.9664E-9	1.0959E-6	9/13 69.2%	952/17866 5.3%
51674	localization of cell	5.5580E-9	1.8586E-6	9/13 69.2%	1071/17866 5.9%
48870	cell motility	5.5580E-9	1.8586E-6	9/13 69.2%	1071/17866 5.9%

Carboxylic acid metabolic process

GO-ID	Description	p-val	corr p-val	cluster freq	total freq
19752	carboxylic acid metabolic process	4.8227E-9	1.2865E-6	7/8 87.5%	869/17866 4.8%
43436	oxoacid metabolic process	9.6609E-9	1.2865E-6	7/8 87.5%	960/17866 5.3%
6082	organic acid metabolic process	1.1155E-8	1.2865E-6	7/8 87.5%	980/17866 5.4%
44281	small molecule metabolic process	5.1445E-7	4.4500E-5	7/8 87.5%	1701/17866 9.5%
32787	monocarboxylic acid metabolic process	1.0372E-6	7.1771E-5	5/8 62.5%	517/17866 2.8%

Viral Process

GO-ID	Description	p-val	corr p-val	cluster freq	total freq
16032	viral process	3.4604E-6	1.0030E-3	4/4 100.0%	772/17866 4..
44403	symbiotic process	5.2101E-6	1.0030E-3	4/4 100.0%	855/17866 4..
377	RNA splicing, via transesterification reactions with bulged adenosine as nucleophile	1.8151E-5	1.4402E-3	3/4 75.0%	298/17866 1..
398	mRNA splicing, via spliceosome	1.8151E-5	1.4402E-3	3/4 75.0%	298/17866 1..
375	RNA splicing, via transesterification reactions	1.8704E-5	1.4402E-3	3/4 75.0%	301/17866 1..

Organelle Localization

GO-ID	Description	p-val	corr p-val	cluster freq	total freq
51656	establishment of organelle localization	2.1016E-7	1.2862E-4	4/4 100.0%	384/17866 2..
51640	organelle localization	1.2347E-6	3.7782E-4	4/4 100.0%	597/17866 3..
30705	cytoskeleton-dependent intracellular transport	4.8493E-6	9.8926E-4	3/4 75.0%	192/17866 1..
47497	mitochondrion transport along microtubule	8.6719E-6	1.0614E-3	2/4 50.0%	22/17866 0....
34643	establishment of mitochondrion localization, microtubule-mediated	8.6719E-6	1.0614E-3	2/4 50.0%	22/17866 0....

Peptidyl-serine Phosphorylation

GO-ID	Description	p-val	corr p-val	cluster freq	total freq
18105	peptidyl-serine phosphorylation	8.9507E-6	3.7657E-3	3/5 60.0%	174/17866 0.9%
18209	peptidyl-serine modification	1.3190E-5	3.7657E-3	3/5 60.0%	198/17866 1.1%
72740	cellular response to anisomycin	2.7986E-4	3.3249E-2	1/5 20.0%	1/17866 0.0%
51403	stress-activated MAPK cascade	3.3180E-4	3.3249E-2	2/5 40.0%	104/17866 0.5%
72739	response to anisomycin	5.5966E-4	3.3249E-2	1/5 20.0%	2/17866 0.0%

Suppl. Fig. 8. BinGO clusters. Markov clustering combined with BinGO gene ontology analysis revealed 8 biologically relevant protein clusters.

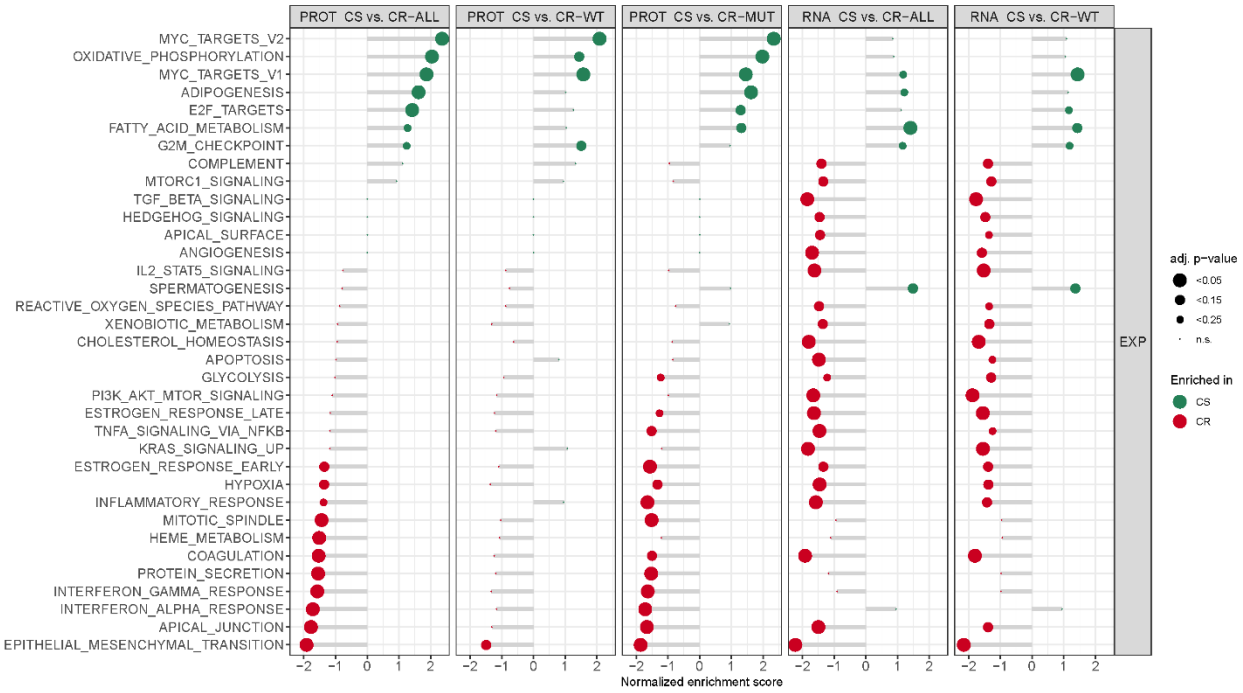

Suppl. Fig 9. Protein and RNA expression-driven enrichment of CS- and CR-specific biology. Lollipop plots showing the normalized enrichment scores of differentially regulated expression-driven HALLMARK signatures between CS and CR PDX models as determined by gene set enrichment analysis (GSEA). The size of the circles correspond to significance of enrichment. Shown are processes that are at least sub-significant (adj. p-value <0.15) in at least one of the comparisons.

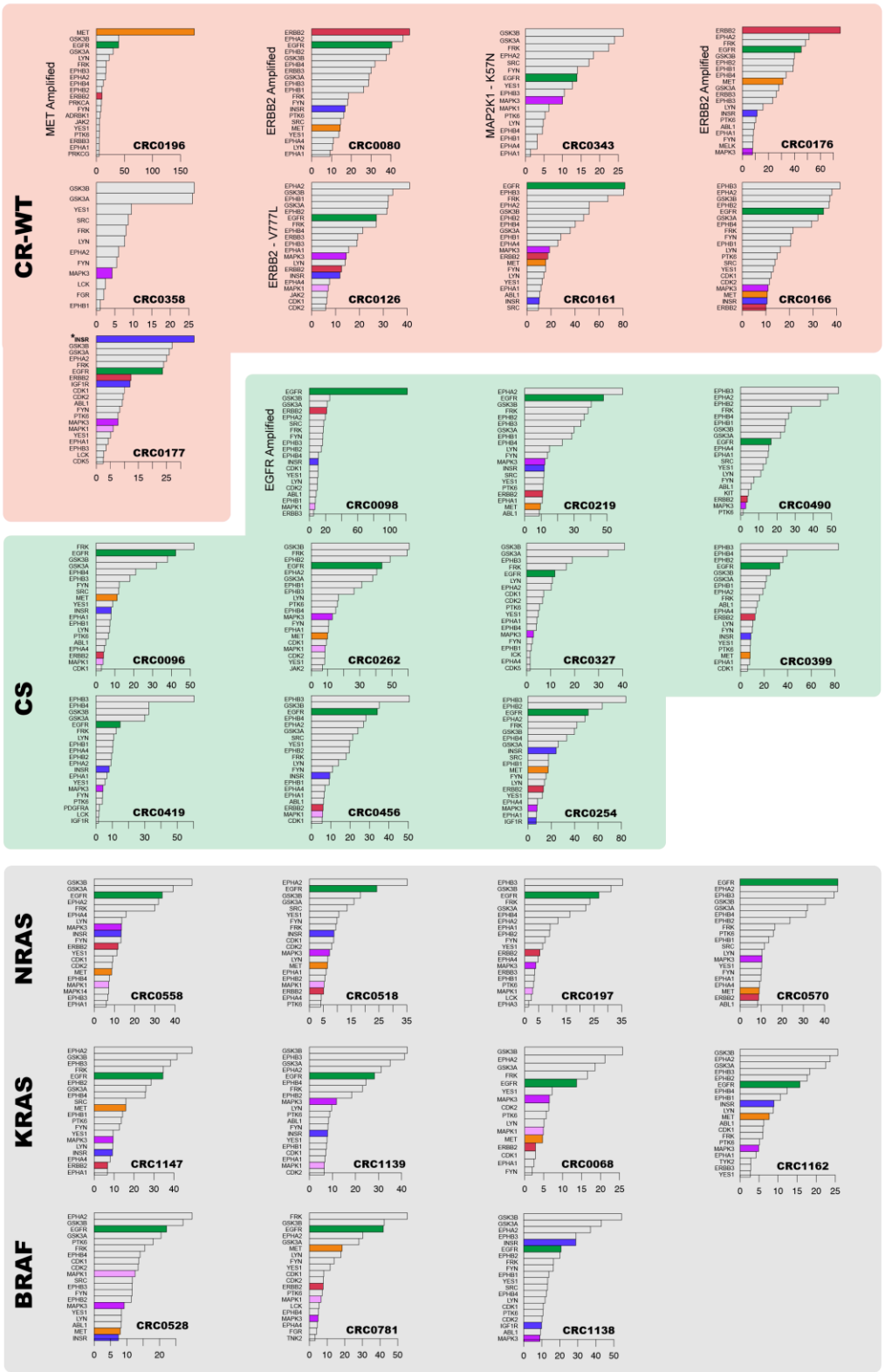

Suppl. Fig. 10. pTyr INKA Bargraph of all PDX-Models. Bargraph show INKA score of all models. EGFR (green), ERBB2 (red), MET (orange), MAPK1 (pink), MAPK3 (purple), and

INSR/IGF1R (blue) are highlighted. (*) In CRC0177 INSR/IGF1R was confirmed as co-target (Beekhof et al., Mol.Sys Bio 2019).

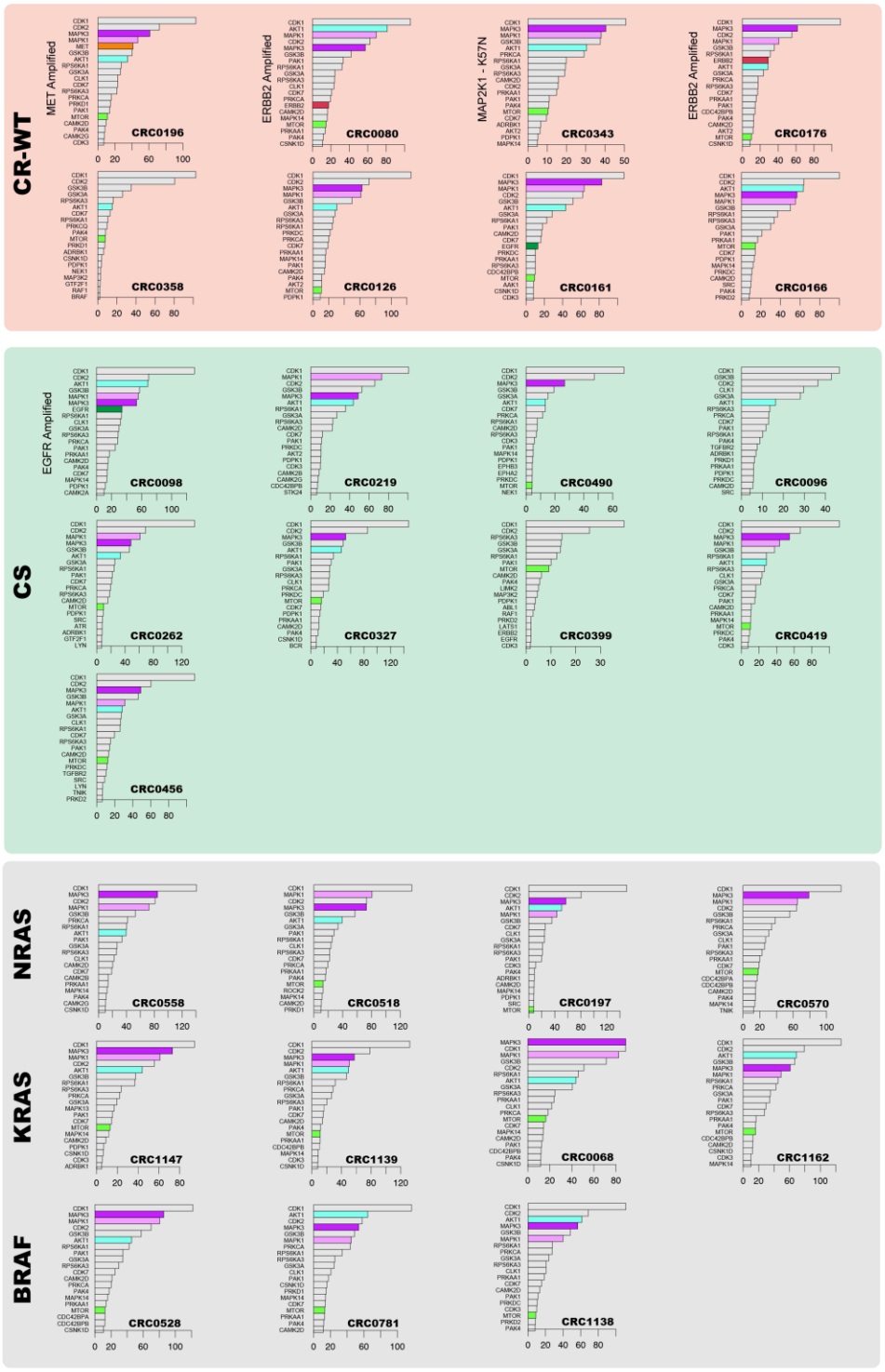

Suppl. Fig.11. TiO2 INKA Bargraph of all PDX-Models. Bargraph show INKA score of all models. EGFR (green), ERBB2 (red), MET (orange), MAPK1 (pink), MAPK3 (purple), MTOR (light green) and AKT1 (light blue) are highlighted.

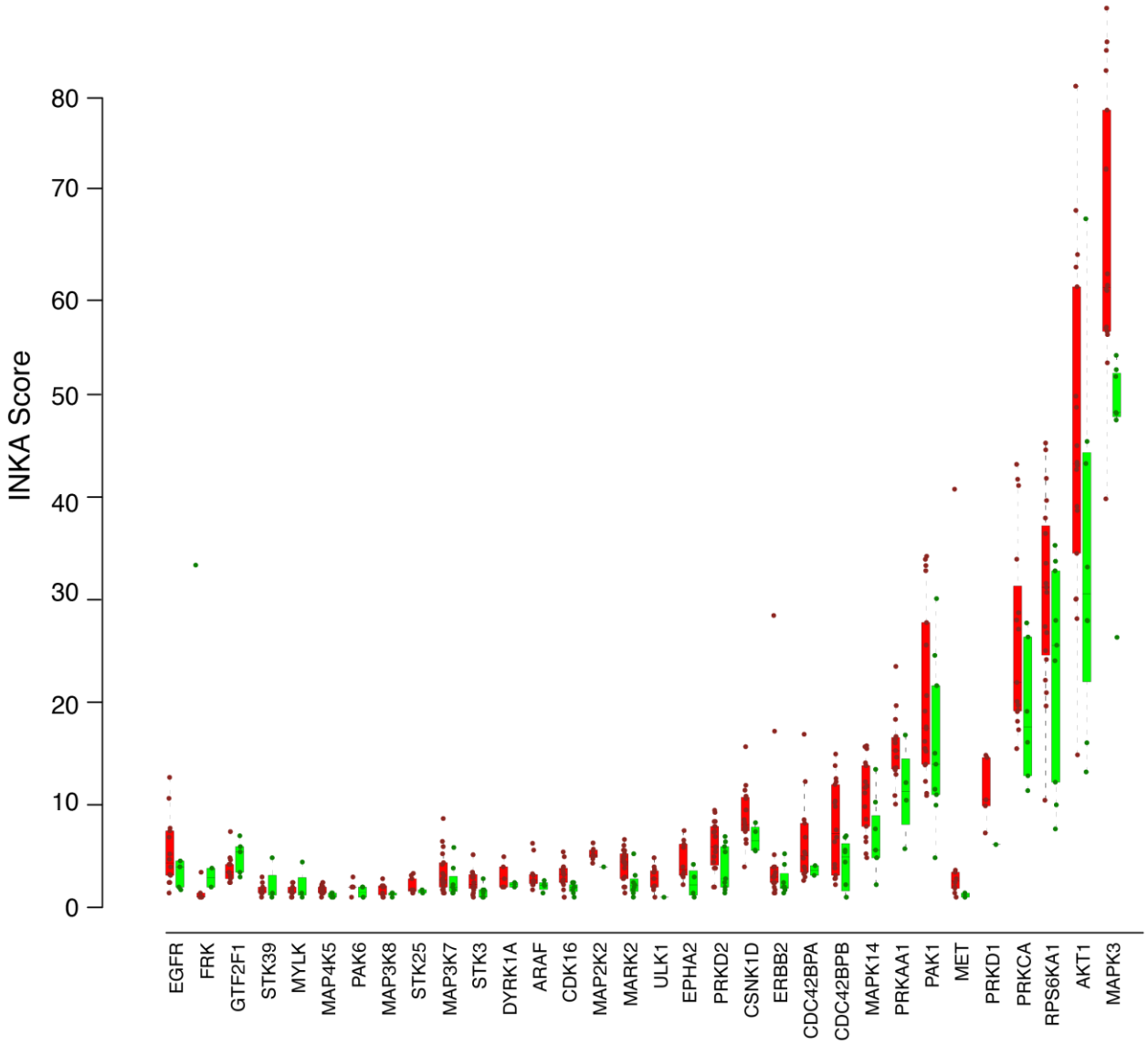

Suppl. Fig. 12. TiO2 mean INKA Bargraph. Boxplot depicting mean INKA score of CS (green) to CR models (red), showing only kinases with more than 25% difference between CS and CR. Kinases must have been measured in more than 5 models. Dots indicate individual PDX models.

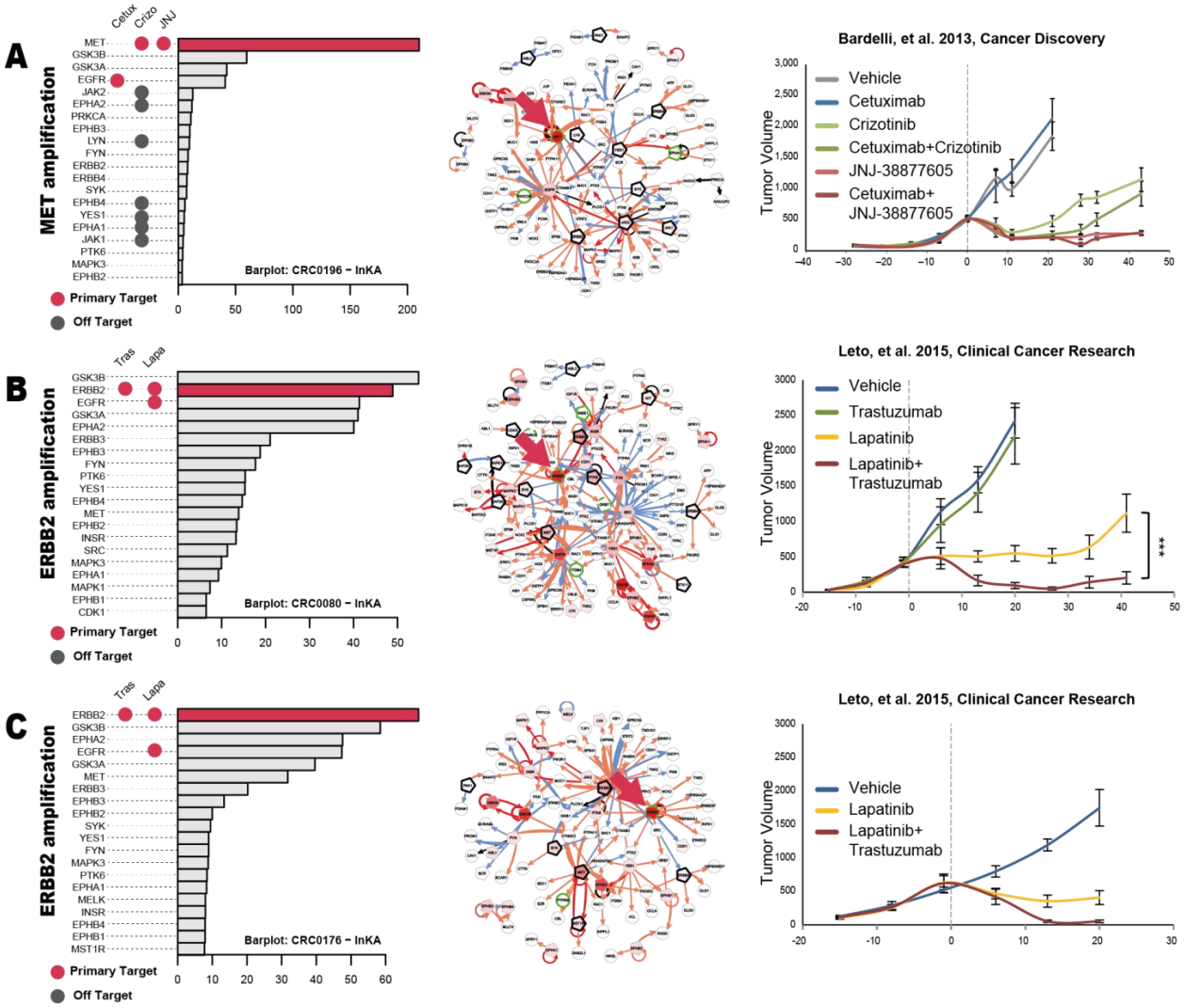

Suppl. Fig. 13. INKA analysis of tumors with known cetuximab resistance trough gene amplification. (A), CRC0196; Left, ranking of top Kinases with their INKA score. Middle, kinase interaction network (red arrow indicates amplified Kinase MET). Right, response to MET inhibitors as described in Bardelli et al., 2013**. (B),** CRC0080; Left, ranking of top Kinases with their INKA score. Middle, kinase interaction network (red arrow indicates amplified Kinase ERBB2). Right, response to ERBB2 inhibitors as described in Bertotti et al., 2015 and Leto et al., 2015**. (C),** CRC0176; Left, ranking of top Kinases with their INKA score. Middle, kinase interaction network (red arrow indicates amplified Kinase ERBB2). Right, response to ERBB2 inhibitors as described in Bertotti et al., 2015 and Leto et al., 2015.

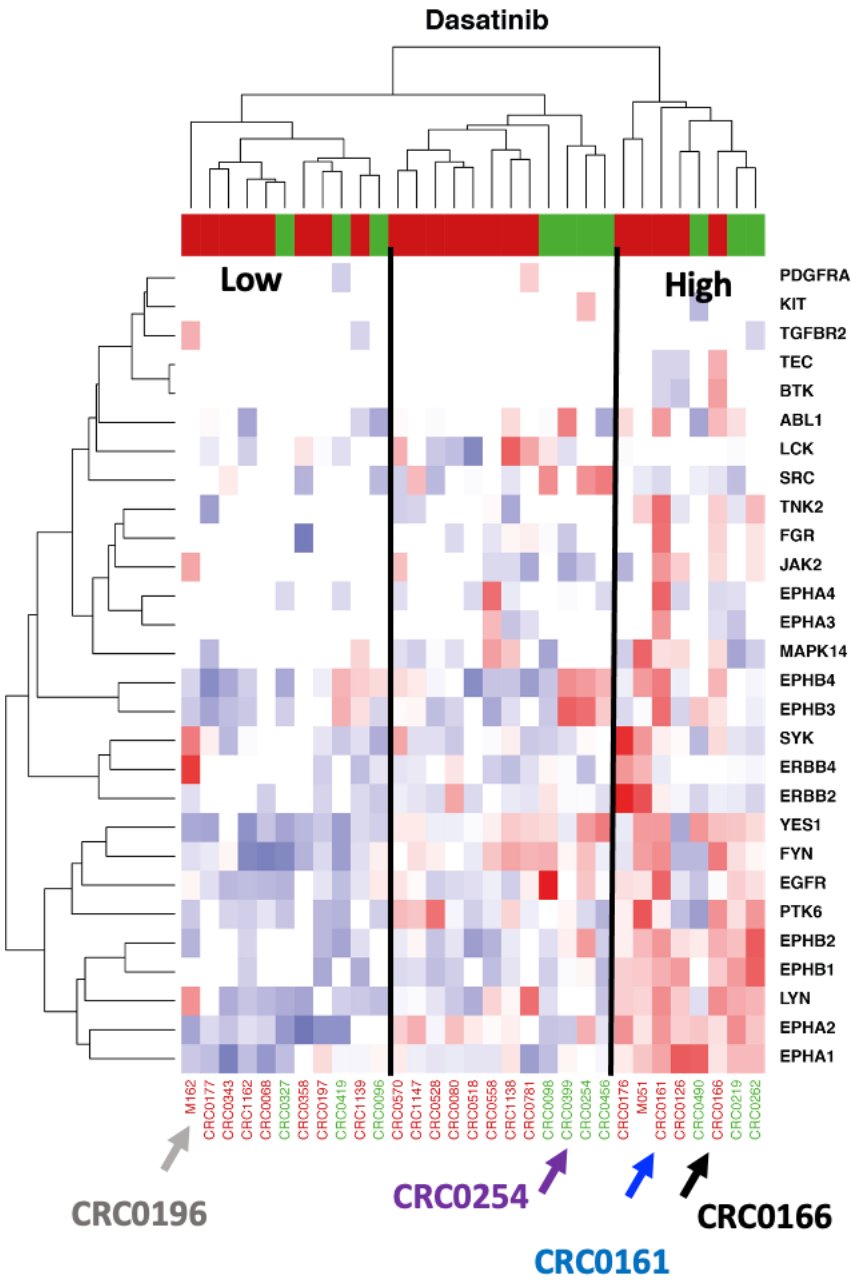

Suppl. Fig. 14. INKA score of Dasatinib targets across all models. Clustering of INKA scores of known Dasatinib targets shows models with relative high score for all targets (CRC0161, CRC0166) and medium to low score (CRC0196, CRC0254). Based on this CRC0196 and CRC0254 where selected as negative control for treatment with Dasatinib.

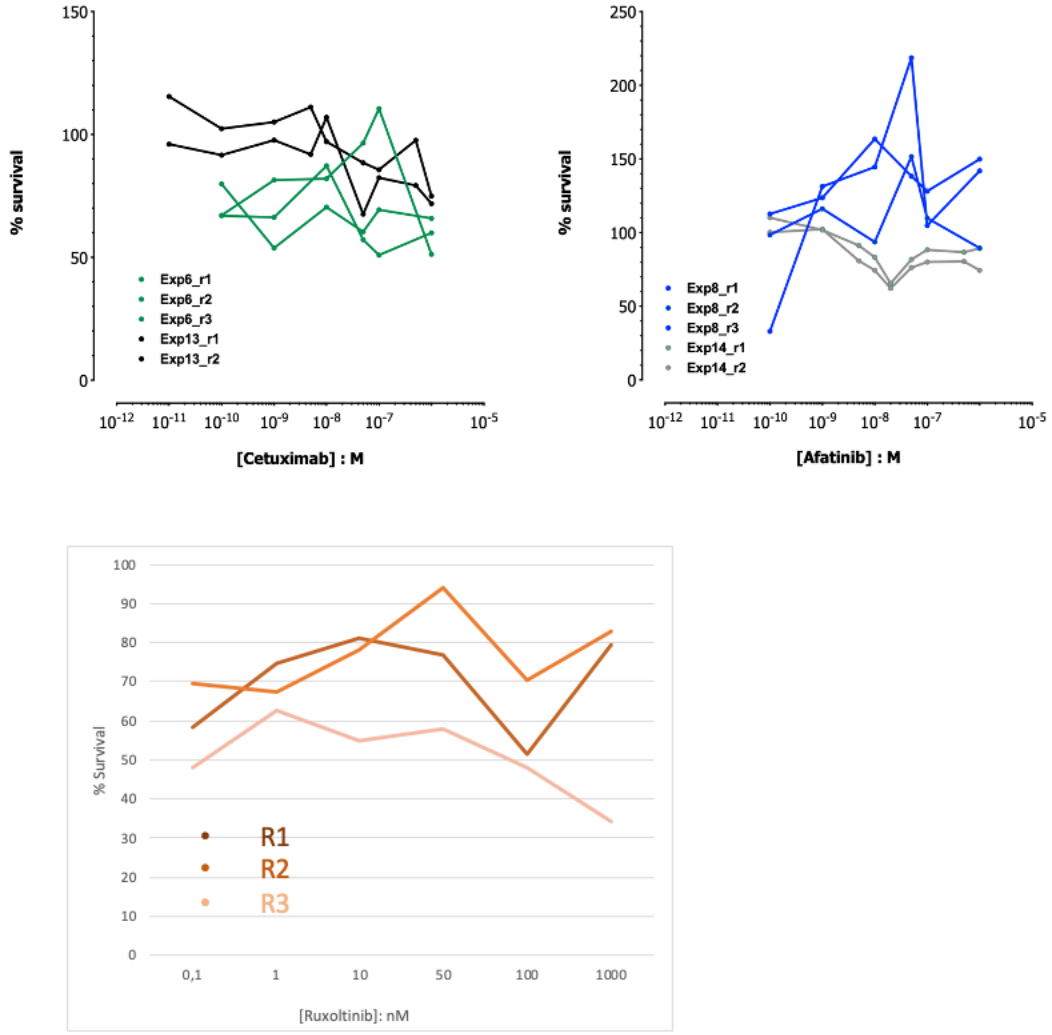

Suppl. Fig. 15. Viability of CRC-0161. Treatment in CRC0161 with cetuximab, afatinib or the inhibition of JAK with ruxolitinib, a "negative control" that did not show high INKA scoring in CRC0161, did not result in reduction of organoid viability.